ARTICLES

Production of direct photons and neutral mesons at large transverse momenta by π^- and p beams at 500 GeV/c

G. Alverson,[6] W. F. Baker,[3] G. Ballocchi,[10,(a)] R. Benson,[5,(b)] D. Berg,[3] S. Blusk,[9] C. Bromberg,[4] D. Brown,[4] D. Carey,[3] T. Chand,[2] C. Chandlee,[10] B. C. Choudhary,[2,(c)] W. H. Chung,[9] L. de Barbaro,[10] W. DeSoi,[10] W. Długosz,[6] J. Dunlea,[10] S. Easo,[8,(d)] E. Engels, Jr.,[9] W. Faissler,[6] G. Fanourakis,[10] T. Ferbel,[10] D. Garelick,[6] G. Ginther,[10] G. Glass,[6] M. Glaubman,[6] P. Gutierrez,[7] K. Hartman,[8,(e)] J. Huston,[4] C. Johnstone,[3] V. Kapoor,[2] I. Kourbanis,[6,(f)] A. Lanaro,[10] C. Lirakis,[6] F. Lobkowicz,[10] P. Lukens,[5,(f)] S. Mani,[1] A. Maul,[4] J. Mansour,[10,(g)] R. Miller,[4] C. A. Nelson, Jr.,[3] B. Y. Oh,[8] D. Orris,[9,(f)] E. Pothier,[6] E. Prebys,[10,(h)] B. M. Rajaram,[2,(i)] R. Roser,[10] K. Ruddick,[5] P. Shepard,[9] R. K. Shivpuri,[2] A. Sinanidis,[6] D. Skow,[10,(f)] P. Slattery,[10] L. Sorrell,[4] W. Toothacker,[8] N. Varelas,[10] D. Weerasundara,[9] J. Whitmore,[8] G. Wu,[6,(f)] T. Yasuda,[6] C. Yosef,[6,(g)] and M. Zieliński[10]

(Fermilab E706 Collaboration)

[1] *University of California–Davis, Davis, California 95616*
[2] *University of Delhi, Delhi 11 00 07, India*
[3] *Fermi National Accelerator Laboratory, Batavia, Illinois 60510*
[4] *Michigan State University, East Lansing, Michigan 48824*
[5] *University of Minnesota, Minneapolis, Minnesota 55455*
[6] *Northeastern University, Boston, Massachusetts 02115*
[7] *University of Oklahoma, Norman, Oklahoma 73019*
[8] *Pennsylvania State University, University Park, Pennsylvania 16802*
[9] *University of Pittsburgh, Pittsburgh, Pennsylvania 15260*
[10] *University of Rochester, Rochester, New York 14627*

(Received 28 December 1992)

We present results from the initial run of Fermilab experiment E706. The data include incident π^- and p beams at 500 GeV/c on Be and Cu targets, and span the kinematic ranges of transverse momentum and rapidity of $3.5 \leq p_T \leq 10$ GeV/c and $-0.7 \leq y_{\text{c.m.}} \leq 0.7$, respectively. We have measured cross sections for π^0 and direct-photon production, as well as the η/π^0 production ratio. From the data on Be and Cu, we have extracted the nuclear dependence of π^0 production, parametrized as A^α. The cross sections are compared with next-to-leading-log QCD predictions for different choices of the QCD momentum scales and several sets of parton distribution functions.

PACS number(s): 13.85.Qk, 12.38.Qk, 13.85.Ni, 25.40.Ve

I. INTRODUCTION

The study of inclusive single-hadron production at large transverse momentum (p_T) has been important to the development of QCD [1, 2]. Large p_T is a regime where perturbative methods can be applied to QCD to provide a quantitative comparison with data. Such comparisons yield information on the validity of QCD matrix elements, and on the effective product of the parton distribution functions of hadrons and the fragmentation functions of partons.

Experimental and phenomenological aspects of direct, or prompt, photon production at large p_T have been addressed extensively in the literature [3]. The production of direct photons at large transverse momentum provides a clean test of perturbative QCD, and can serve as a valuable tool for probing hadronic structure. To first order, only the two processes shown in Fig. 1 contribute to

[a] Current address: CERN, 1211 Geneva 23, Switzerland.
[b] Current address: LeCroy Corporation, Chestnut Ridge, NY 10977.
[c] Current address: University of California, Riverside, CA 92521.
[d] Current address: INFN, University of Perugia, Perugia, Italy.
[e] Current address: Stanford University, Stanford, CA 94309.
[f] Current address: Fermi National Accelerator Laboratory, Batavia, IL 60510.
[g] Current address: Michigan State University, East Lansing, MI 48824.
[h] Current address: Princeton University, Princeton, NJ 08544.
[i] Current address: L. B. and S. B. S. College, Sagar, Karnatka 577401, India.

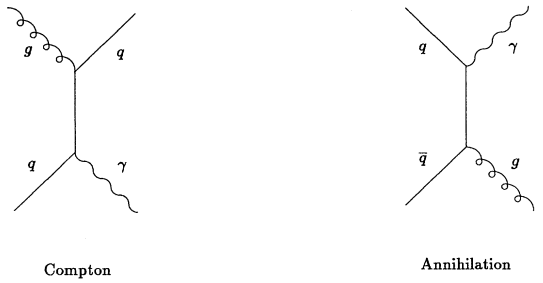

FIG. 1. Lowest order diagrams for direct-photon production.

the direct-photon cross section, namely, $q\bar{q}$ annihilation and quark-gluon Compton scattering. These diagrams capture the essential characteristics of the process, and relatively unambiguous higher-order calculations can be carried out to provide precise tests of theory [4]. Since the photons from the processes shown in Fig. 1 are produced at the elementary vertex of the interaction, and not in the fragmentation of an outgoing parton, the momentum of the photon directly reflects the kinematics of the collision. This is in contrast with jet production, in which the hadronization process obscures the measurement of the energy and direction of the outgoing parton. Because of the presence of an intial state gluon in the Compton diagram, prompt photon data are especially sensitive to the gluon distribution functions. In combination with deep inelastic scattering and Drell-Yan production, direct-photon data can be used to map out the gluon distribution function over a wide range of kinematics.

Previous measurements of direct-photon production have covered a variety of center-of-mass energies and incident beam particles [5–7]. Our measurements provide the highest energy data for pion beams, and straddle results on proton interactions obtained previously at the CERN Intersecting Storage Rings (ISR) [6] and in earlier fixed-target experiments [7].

In the following sections we describe the experimental layout and the analysis procedures used to extract the π^0 and direct-photon signals. The results on direct-photon and π^0 production are compared with predictions from next-to-leading-log QCD calculations. The results presented in this paper expand upon more abbreviated recent publications of our work [8], and provide detailed comparisons with QCD predictions at the next-to-leading-log level for both π^0's and direct photons.

II. THE EXPERIMENTAL SETUP

Fermilab experiment E706 is a second generation fixed-target experiment designed to measure direct-photon production and the associated event structure. To this end a liquid-argon electromagnetic calorimeter (EMLAC) with fine segmentation was used to optimize the reconstruction of overlapping photons (particularly from π^0 decays, a large source of background to the direct-photon signal). The EMLAC was split into front and back sections to provide discrimination against hadrons. A charged-particle tracking system was used to identify showers in the EMLAC that were initiated by charged particles, and to reconstruct interaction vertices. Figure 2 shows the layout of the various components of the Meson West spectrometer. This spectrometer was employed simultaneously by experiments E706 and E672 [9]. The spectrometer components are discussed in the following subsections.

A. Beam line

The Meson West secondary beam line is a high resolution, two stage, momentum recombining beam line. It is capable of delivering a high intensity beam with mass tagging. The secondary particles utilized in the experiment were produced by 800 GeV/c protons, extracted from the Fermilab Tevatron, incident upon an 0.77-interaction-length aluminum primary target. The components of this beam line are shown in Fig. 3.

For the data presented here, the secondary beam energy was tuned to 500 ± 29 GeV/c (rms half-width). The beam was occasionally tuned to 25, 50, and 100 GeV/c for detector calibration purposes. The negative secondaries were produced at an angle of 0 mr to maximize the yield, which for this run was 2×10^{-5} per primary proton. For positive particles, the production angle was 1.4 mr to prevent the intense primary proton beam from entering the secondary beam-line aperture. The positive particle yield was 10^{-4} per primary proton. The Tevatron operated on a 57-s cycle, with a 23-s spill, during which the experiment typically received 5×10^7 secondary beam particles.

The intermediate focus of the beam was momentum dispersed in the horizontal plane. The momentum defining collimator was located at this intermediate focus. The final focus, at the experiment target, was momentum recombined. The second stage of the beam line included a 50-m-long straight section, in which the trajectories were parallel in both the horizontal and vertical planes. This section contained a differential Cherenkov counter used to identify the masses of the incident particles. The counter used a 42-m-long helium-gas radiator in the pressure range from 4 to 7 psi (absolute). Using this device, the negative beam was found to contain 97% π^- and 3% K^- while the positive beam was measured to contain 91% p, 7% π^+, and $< 2\%$ K^+ [10].

The beam line contained five muon spoilers, constructed of magnetized steel. Their function was to deflect muons in the beam halo away from the spectrometer. A 5-m-long hadron absorber, composed of 900 tons of steel, surrounded the beam just upstream of the target in the experimental hall. Its purpose was to absorb hadrons in the beam halo. Two large walls of scintillation counters (referred to as veto walls in Fig. 2) were positioned between the hadron absorber and the target to veto events generated by any remaining beam halo particles.

B. Charged-particle tracking system

The experiment utilized a charged-particle tracking system consisting of silicon strip detectors (SSD's), an

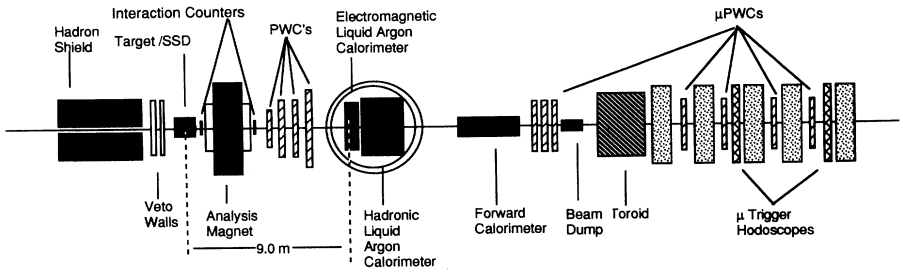

FIG. 2. Layout of the Fermilab Meson West spectrometer as employed in the initial (1987–1988) run.

analysis magnet, and proportional wire chambers. Six SSD planes were located upstream of the target and used to reconstruct beam tracks. Eight SSD planes were located downstream of the target and were used to reconstruct the interaction vertex. The analysis magnet, which imparted a transverse momentum impulse (in the horizontal plane) of $\approx 450\,\mathrm{MeV}/c$ to charged particles, was followed by 16 planes of proportional wire chambers (PWC).

The SSD system was constructed of seven X-Y modules, with two planes per module [11]. The three modules upstream of the target, and the first one downstream, consisted of $3 \times 3\,\mathrm{cm}^2$ wafers, while the remaining modules had $5 \times 5\,\mathrm{cm}^2$ wafers. All the SSD's were 250 to 300 μm thick, and had a pitch of 50 μm. There were a total of 6600 instrumented SSD channels.

The PWC system consisted of four modules, with four planes per module [12]. Each of the four modules had one X, Y, U, and V view. The wires in the U view were tilted at 37°, and in the V view at −53°, relative to the vertical. The sense wires had a pitch of 0.254 cm. The active areas of the four modules were 1.22 m×1.22 m, 2.03 m × 2.03 m, 2.03 m × 2.03 m, and 2.44 m × 2.44 m, and covered the accepted region of the liquid-argon calorimeters. The central region high voltage of each PWC plane was fed through a current limiting resistor which reduced the sensitivity of that region during high intensity running. The desensitized area varied from 2.54 cm × 2.54 cm in the first PWC module to 5.08 cm × 5.08 cm in the last PWC module. There were a total of 13 400 instrumented PWC channels. The combined PWC and SSD system was designed to operate at a 1-MHz interaction rate.

C. Liquid-argon calorimeter

The next element in the experiment was a 3-m diameter liquid-argon calorimeter (LAC) [13], consisting of an electromagnetic (EMLAC) section ($\approx$ 30 radiation lengths) followed by a hadronic (HALAC) section ($\approx$ 8 interaction lengths). Together, the calorimeters resided in a stainless-steel cryostat, supported by a gantry that could be moved transverse to the beam axis. The calorimeters were centered on the beam line, with the front end of the EMLAC located $\approx$ 900 cm downstream of the target. The active area covered a polar angle range of $1.3° < \theta < 10°$ as seen from the target. Within the cryostat, a 40-cm-diameter beam pipe, filled with helium gas, was inserted through the center of both calorimeters to minimize interactions in this region. In front of the electromagnetic section was a low density ($0.07\,\mathrm{g/cm}^3$) liquid-argon excluder used to minimize energy loss prior to the active region of the LAC.

The electromagnetic section of the LAC consists of four independent quadrants, as shown in Fig. 4. Each quadrant was constructed of 66 layers, with each layer con-

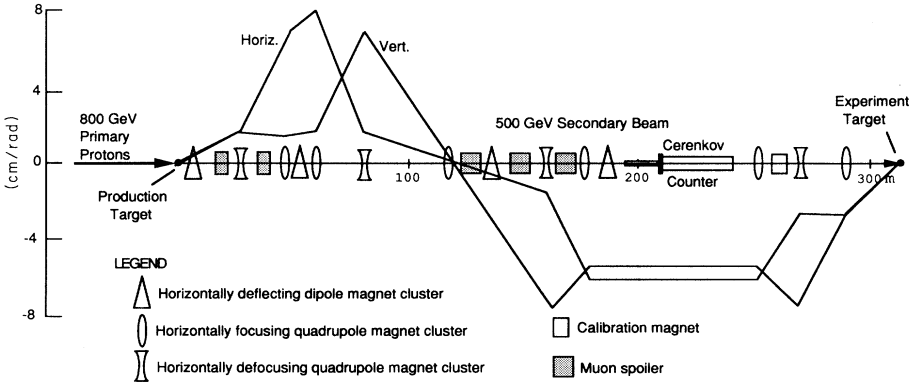

FIG. 3. The Meson West secondary beam line. Horizontal and vertical trajectories for central momentum particles produced at finite production angles illustrate the location of the two foci of the beam as well as the long parallel section for the Cherenkov counter. The calibration magnet was used to sweep the beam vertically over the calorimeter during dedicated calibration runs. Trim magnets (used to align the beam), collimators, and beam-line instrumentation are not shown.

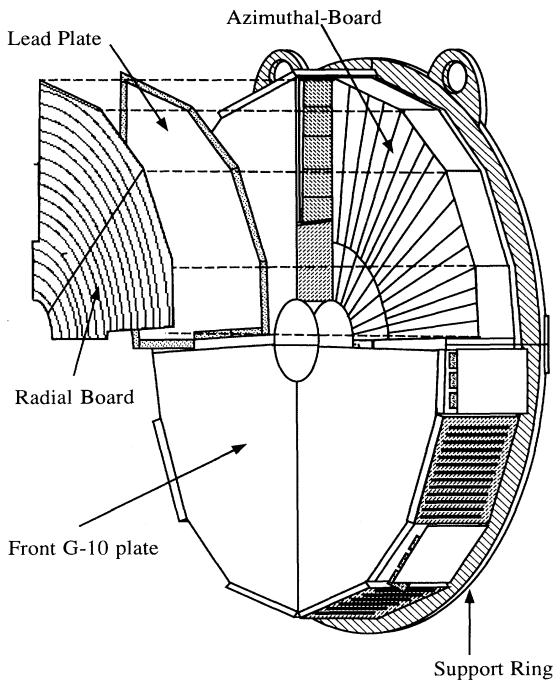

FIG. 4. Detailed view of the EMLAC showing the alternating radial and azimuthal geometries of the readout boards. Also shown is a stainless-steel support ring located on the back of the EMLAC.

sisting of an absorber, 0.25 cm of liquid argon, a copper-clad G-10 anode board, and another 0.25 cm argon gap. The absorber in the first layer was aluminum while for all other layers it was a 0.2-cm-thick lead sheet. The lead sheets were made of 98.6% lead, 0.07% calcium, and 1.3% tin; the calcium and tin were added to increase the mechanical rigidity of the lead sheets.

The G-10 anode boards were octant size, with each octant read out independently. The anode boards had alternating radial and azimuthal strip geometry starting with a radial board. The radial boards consisted of a maximum of 254 strips, cut to be focused (in a projective geometry) on the target. The width of the strips on the first radial layer was ≈ 5.5 mm. The azimuthal boards were divided into an inner region, containing 92 instrumented strips, each subtending $\pi/192$ radians in azimuth, and an outer region containing 188 instrumented strips each subtending $\pi/384$ radians in azimuth (see Fig. 4). The inner-outer separation (at a radius of 40.2 cm on the first readout board) allows for improved spatial resolution at large radii by subdividing the outer strips by a factor of 2. The inner-outer split also aids reconstruction by reducing radial and/or azimuthal correlation ambiguities arising from multiple showers in the calorimeter.

Longitudinally, the calorimeter is read out in two sections. The front section consists of 22 layers (about 10 radiation lengths), while the back consists of the remaining 44 layers. This front-back split is used to measure the direction of incidence of the showering particle and to help discriminate between electromagnetic and hadronic showers.

D. Readout system for the electromagnetic calorimeter

Data acquisition and trigger-signal processing for the EMLAC was performed using the RABBIT (redundant analog bus-based information transfer) system developed by the Particle Instrumentation Group at Fermilab [14]. The liquid-argon calorimeter amplifier (LACAMP) consisted of 16 channels of charge integrating amplifiers and eight channels of time-to-voltage converters. The LACAMP's were located in 20 crates with $\approx$ 20 amplifiers per crate; the crates were positioned within a shielded Faraday room surrounding the circumference of the top of the cryostat. The outputs from the LAC amplifiers consisted of voltage signals proportional to the amount of charge deposited on their respective strips in the calorimeter. The rise time for signals in the EMLAC was $\approx$ 350 ns. The output from each LAC amplifier channel was delayed by 800 ns, giving the trigger the time required either to accept or reject the event. When an event satisfied the trigger, each channel was sampled twice, once before the delayed pulse and once at the peak of the delayed pulse. This voltage difference was digitized by one of two digitizers per crate, provided that the absolute value of the voltage difference was greater than a predefined threshold (the zero suppression window) stored on the digitizer. If no digitization took place because the voltage difference fell within the zero suppression window, the channel was flagged as not having useful data, and the data acquisition system then proceeded to the next channel.

Timing information was provided through the time-to-voltage converters (TVC's) on the LACAMP's. Their function was to produce a voltage proportional to the time between the beginning of a LAC pulse and the trigger signal. The signal used for this timing measurement was generated by summing the output of four consecutive amplifier channels. To avoid dead time caused by the arrival of a second pulse prior to the readout of the TVC, a second (slave) TVC circuit was enabled while the first was busy.

E. Trigger system

The trigger, which selected events depositing high transverse momentum (p_T) in the EMLAC, was designed to operate at 10^6 interactions per second. The trigger p_T was formed by weighting the energy in the radial strips according to the distance from the center of this strip to the beam line ($E \sin\theta$). The triggering process took place in four steps, which involved defining a beam particle, an interaction, a pretrigger, and a final trigger. Figure 5 shows the symbolic logic diagram for the SINGLE LOCAL trigger used in this analysis, whose elements are discussed below.

Beam definition. Two 1/16 in. $\times$1 in. $\times$1 in. scintillation counters located upstream of the target were used to define beam particles. A beam particle was accepted if both counters had a signal in coincidence.

Interaction definition. Four scintillation counters, located downstream of the target and covering the accep-

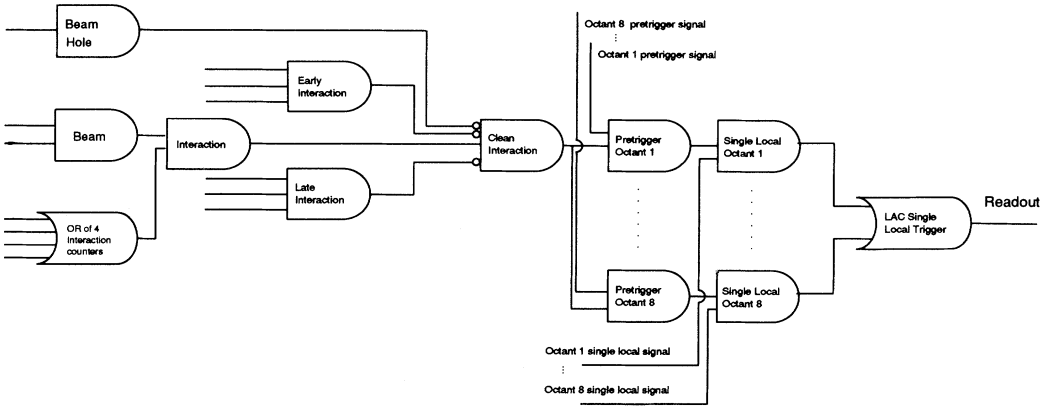

FIG. 5. Symbolic logic requirements for the SINGLE LOCAL trigger used in this analysis.

tance of the spectrometer, were used to define an interaction. The logical OR of the four counters was taken in coincidence with the beam definition to define an interaction. An interaction strobe was generated and used in the definition of the pretrigger if this interaction candidate satisfied the following criteria.

(i) No other interaction occurred within ± 60 ns of this candidate interaction.

(ii) The interaction was not initiated by a particle in the beam halo; that is, there was no signal in the "halo" scintillation counter located just downstream of the two beam defining counters. This 5 in.$\times$5 in. halo counter had a 3/8 in. diameter hole cut out of its center and was centered on the beam.

Pretrigger definition. Signals were generated for the inner and outer parts of each octant using the sums of the weighted energies in the radial strips. These signals were passed through zero-crossing discriminators, which served to define a pretrigger threshold ($\approx 1.7\,\mathrm{GeV}/c$) and to set a more precise pretrigger time (± 75 ns) than would normally be available for the intrinsically slow signals of the LAC.

The logical OR's of the discriminated zero-cross outputs from the inner and outer parts of each octant were used to obtain a pretrigger signal for that octant. The following additional requirements were placed on the final formation of a pretrigger for any octant: no p_T deposition in that octant greater than $1.5\,\mathrm{GeV}/c$ within ≈ 300 ns prior to the interaction; absence of a noise spike generated by the 400-Hz power supplies for the LAC electronics; no incident muon as defined by the logical AND of the signals from the two veto walls. This pretrigger signal was used to latch the LAC, PWC, and SSD signals. The presence of a pretrigger was required for any subsequent trigger.

Trigger definition. The two main triggers used to select events containing electromagnetic showers of high p_T were (1) The SINGLE LOCAL trigger, in which the p_T in a localized region of an octant (16 radial strips) was required to be above a given threshold ($\approx 4\,\mathrm{GeV}/c$) and (2) the LOCAL*GLOBAL trigger, in which the local threshold for an octant was $\approx 2\,\mathrm{GeV}/c$, and a GLOBAL threshold (summed over the whole octant) was simultaneously required ($\approx 4\,\mathrm{GeV}/c$). The LOCAL requirement suppressed events that contained only low-p_T photons. The LOCAL*GLOBAL trigger ensured that π^0 or η events, that had too large an opening angle between their two decay photons to occupy any single LOCAL region, would trigger. A prescaled LOCAL*GLOBAL trigger with a reduced GLOBAL threshold ($\approx 2.5\,\mathrm{GeV}/c$) was also recorded. In addition, a TWO-GAMMA trigger was formed by requiring two local signals, one from any octant and the other from any of the three corresponding away-side octants; a reduced value for the LOCAL threshold ($\approx 2\,\mathrm{GeV}/c$) was employed for this TWO-GAMMA trigger. The variety of trigger definitions with different threshold requirements allowed a measurement of trigger efficiencies as a function of p_T.

If a LAC trigger was satisfied, a signal was sent to the on-line computers to initiate the recording of the information for the event. Otherwise, a reset signal was sent to the various electronic modules. The trigger circuitry then allowed a settling time of ≈ 30 μs before being enabled for the next pretrigger.

III. DATA ANALYSIS

During the 1987–1988 Fermilab fixed target run, a sensitivity of approximately 0.5 (0.8) events/pb was accumulated with negative (positive) beam on Be; data on Cu corresponded to about 10% of the Be sample. Only events which satisfied the SINGLE LOCAL trigger were included in the present analysis. The events were reconstructed off-line using the Fermilab ACP [15] system. The following subsections will describe the event reconstruction procedures and the methods used to correct the data for losses due to various inefficiencies and biases.

A. Event reconstruction

The event reconstruction procedure for this experiment included charged-particle track reconstruction and electromagnetic shower reconstruction. We discuss these procedures in the following paragraphs.

Charged-particle tracking. The charged-track recon-

struction algorithm formed independent track segments, upstream of the magnet using the SSD planes, and downstream of the magnet using the PWC planes. These segments were then linked at the center of the magnet to form the final reconstructed track.

The first step in reconstruction involved forming straight-line segments in each of the four views (X, Y, U, V) of the PWC's, and in each of the two views (X, Y) of the SSD's. A "view track" was defined in the PWC's when at least three out of the four available planes had hits associated with the track. In order for a hit to be associated with a track it had to lie within ± 1.5 wire spacings of the trajectory. Tracks in three-dimensional coordinates, termed "space tracks," were formed using the view tracks. A maximum of 16 hits (4 planes and 4 views) could be associated with a track. A space track had to have a total of at least 13 hits within ± 1.5 wire spacings of the trajectory.

After reconstruction of the PWC space tracks and SSD view tracks, each of the PWC tracks and SSD tracks were projected to the X-Y plane at the center of the magnet. After accounting for the effects of the magnetic field, SSD and PWC tracks that corresponded spatially at the center of the magnet were considered candidate linked tracks. Since the magnet caused deflections primarily in the X-Z plane, the slopes of the linked tracks in the Y view were also required to match to within 2.5 mrad. The charge and momentum of each linked track was then calculated.

The interaction vertex position was reconstructed separately in each view (X and Y), and then correlated by requiring a match in the Z coordinate. For each SSD view, tracks that linked with PWC tracks were preferentially employed to reconstruct the vertex. Unlinked SSD view tracks were also used if an insufficient number of linked tracks were present. The final interaction vertex position was determined by the pair of view vertices that matched best in the Z coordinate.

Electromagnetic shower reconstruction. Electromagnetic showers were reconstructed independently for each quadrant. The readout in each quadrant consisted of four "views": left R and right R, containing the energies in the radial strips of each octant in that quadrant, and inner Φ and outer Φ, containing the energies in the azimuthal strips for $r < 40.2$ cm and for $r > 40.2$ cm, respectively. The reconstruction algorithm operated in the following sequence: first, a search was performed, within each view, for energy depositions, termed "groups" and "peaks" (defined below); second, the energies and positions of these peaks were calculated by fitting to a predetermined shower shape; third, photons were reconstructed by correlating peaks from different views.

A group was defined as consisting of consecutive strips, each with energy above 150 MeV, and with at least one strip with energy above 300 MeV, and a total group energy of more than 750 MeV. A peak was defined by a sequence of strips within a group that had energy minima ("valleys") on both sides of a maximum value, such that the maximum value was more than $2.5\,\sigma$ above the valleys. Each peak was fitted to the shape of an electromagnetic shower determined from Monte Carlo simulations and tuned to match showers in the data. The results of that fit include the position and energy of the peak. Photons were formed by correlating peaks of approximately the same energy in the R and Φ views. Peaks from different views were required to occupy the same general region of the detector, namely, a radial peak with $r < 40.2$ cm ($r > 40.2$ cm) could only be correlated with inner (outer) Φ peaks, and a peak in the Φ view could only be correlated with a radial peak in the octant containing that ϕ value.

The correlation routine in the electromagnetic reconstruction algorithm may fail for complicated events containing a large number of photons, leaving a large amount of uncorrelated energy (not associated with any photon). Such events were eliminated by requiring the total uncorrelated energy for the triggering quadrant to be less than 10 GeV.

A relative interaction time was calculated for photons based on information obtained from the TVC channels of the amplifiers corresponding to that photon's energy deposition.

B. Single-photon and di-photon identification

Two of the largest potential sources of background to the direct-photon signal are from bremsstrahlung of beam halo muons in the outer regions of the EMLAC and from electromagnetic decays of π^0 and η mesons. The majority of the muon background (from beam halo) was eliminated by requiring that no hit register in the section of the veto wall that overlapped (shadowed) the region of the electromagnetic calorimeter that satisfied the trigger. An off-line reconstructed vertex was also required for each accepted event.

Figure 6 displays the $\gamma\gamma$ invariant mass in the π^0 and η mass ranges for SINGLE LOCAL triggers, requiring a p_T of at least 3.5 GeV/c for the two-photon pairs. The π^0 energy asymmetry is defined as $A = |E_{\gamma_1} - E_{\gamma_2}|/[E_{\gamma_1} + E_{\gamma_2}]$, where E_{γ_1} and E_{γ_2} represent the energies of the photons. The lower points, with the dashed error bars, represent the mass spectrum for $A < 0.75$. For our study of π^0 production, a π^0 was defined as any two-photon combination with $A < 0.75$, and invariant mass $M_{\gamma\gamma}$ in the range $110\,\mathrm{MeV}/c^2 < M_{\gamma\gamma} < 160\,\mathrm{MeV}/c^2$. Both photons were required to occupy the same octant. An η was defined as any two-photon combination with $A < 0.6$ (for direct-photon background estimates this requirement was $A < 0.75$) and $450\,\mathrm{MeV}/c^2 < M_{\gamma\gamma} < 650\,\mathrm{MeV}/c^2$. The minimum p_T value employed in the analysis was determined by the trigger threshold used during the corresponding data acquisition period. To account for combinatorial background under the π^0 and η signals, sidebands were selected which covered the equivalent mass range of the π^0 and η peaks. Distributions from these sidebands were then subtracted from the distributions within the π^0 and η mass ranges to obtain the respective signals.

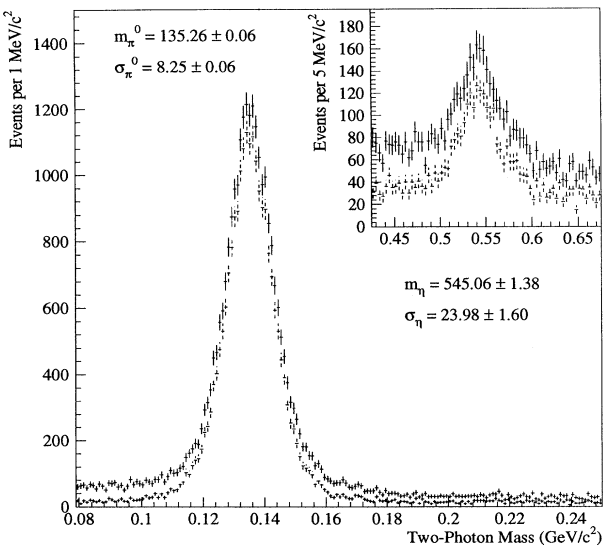

FIG. 6. Two-photon invariant-mass distribution in the π^0 and η (insert) mass regions. The lower, dashed points represent $\gamma\gamma$ pairs with energy asymmetry < 0.75. A p_T requirement of 3.5 GeV/c on each two-photon pair has also been applied.

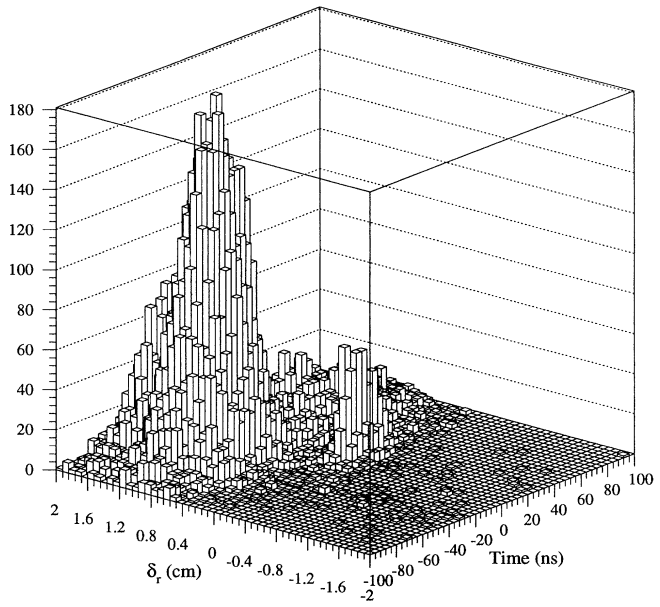

FIG. 7. Lego plot of the time vs directionality of single photons with $p_T > 3.5$ GeV/c when the veto wall had a signal in an area corresponding to the triggering octant of the calorimeter. Note the large number of out-of-time photons with large directionalities indicating particles were incident parallel to the beam line.

A photon was a direct-photon candidate if it did not combine with another photon in the same octant to form a π^0 or η with an $A < 0.75$. The residual background from π^0's and η's was calculated using our Monte Carlo simulation program, which will be discussed in a following section. The minimum p_T value in the analysis was again chosen to correspond to the trigger threshold set in each particular running period.

We defined a directionality parameter for photons as

$$\delta_r = r_f - \frac{z_f}{z_b} r_b, \tag{1}$$

where r_f and r_b are the reconstructed front and back radial positions of the shower and z_f and z_b are the distances of the front and back sections of the electromagnetic calorimeters to the target. Photons originating from the target have directionality close to zero, while showers from muons traveling parallel to the beam line have large positive directionalities.

Directionality and in-time requirements were imposed on all direct-photon candidates in order to minimize background from muon bremsstrahlung events that passed the veto wall criteria when an interaction vertex was found. In cases where the photon time or directionality could not be reconstructed, they were assumed to be in-time and have good directionality. Showers not originating from the target are frequently out of time with the interaction. Figures 7 and 8 show plots of the single-photon arrival time at the EMLAC versus directionality, for events with and without a signal in the veto wall (in the region corresponding to the triggering octant). Requiring a signal in the veto wall produces a large concentration of out-of-time showers (muons) that also have large directionality. Applying the veto wall requirement eliminates most of these showers, leaving essentially only in-time showers (photons) originating in the target region.

To eliminate possible electron or hadronic background to the direct-photon signal we required that accepted showers not spatially overlap with any charged track projected to the LAC (within 1 cm of the center of the shower), and that at least 20% of each shower's energy be contained in the front section of the electromagnetic calorimeter ($E_f/E_t > 0.2$). Note that this track projection cut serves to reject electrons (and showering charged hadrons) and is not an isolation cut in the sense employed in collider measurements of direct-photon cross sections. This track projection cut eliminates $\approx 8\%$ of the candidate single-photons from our sample.

C. Energy scale

Due to the steep p_T dependence of inclusive cross sections, a small change in the energy scale of the EMLAC can produce large changes in the measured cross section at a specific energy. Because of this sensitivity, the energy scale must be determined with great care. One possible procedure is to set the energy scale such that the reconstructed π^0 mass is centered at the accepted value. This method can be compromised by the sensitivity of the reconstructed mass value to the degree of overlap of the two-photon showers originating from π^0 decay. Instead, we set the energy scale using events in which one of the photons from a π^0 decay converted into an e^+e^- pair upstream of the magnet. Using these events, the energy scale in the EMLAC can be calibrated from reconstructed

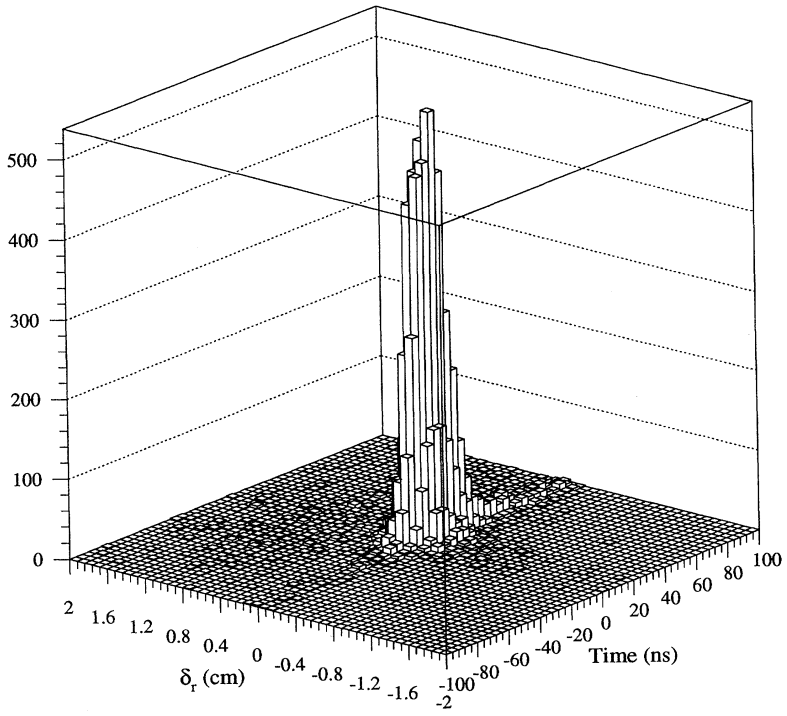

FIG. 8. Lego plot of the time vs directionality of single photons with $p_T > 3.5\,\mathrm{GeV}/c$ when no veto wall element had a signal in an area corresponding to the triggering octant of the calorimeter. Note that the vast majority of the events are in time and have directionality consistent with particles originating in the target.

charged-particle momenta. Before describing the different corrections applied to reconstructed photons we will describe how the momentum scale of the tracking system was established.

The tracking system was calibrated using the decays $K_S^0 \to \pi^+\pi^-$ and $J/\psi \to \mu^+\mu^-$. The $J/\psi \to \mu^+\mu^-$ events were selected by the E672 [9] dimuon trigger and identified by the muon spectrometer. K_S^0 decays were obtained from secondary vertices that had two tracks of opposite curvature, with an invariant mass close to that of a K_S^0, when these tracks were interpreted as pions. Figures 9 and 10 show the $\pi^+\pi^-$ mass distribution for events in the K_S^0 mass region and $\mu^+\mu^-$ mass distribution in the J/ψ mass region.

The first energy correction for showers detected in the EMLAC involved taking account of the difference between the pedestals estimated from the data and the pedestals determined from calibration tasks frequently carried out at the start of a run. A fit was performed to the tails of the pulse height distribution in each channel (when no peak was detected by the electromagnetic reconstruction code) to determine the mean pedestal levels expected in the data. Special events, requiring only a beam definition (and no interaction), were used for this purpose in order to minimize biases caused by the presence of energy in the calorimeter. Pedestal differences as large as 250 MeV were observed for some channels. However, these shifts were found to be stable over the course of the data taking, and consequently a single set of pedestal shift corrections was used for all the data.

The next correction was for variations in the energy scale caused by octant-to-octant differences in the LAC. This correction was implemented by rescaling the photon energies in each octant by a factor based on the reconstructed π^0 mass for that octant. Octant-to-octant variations had a range of 6%. Only π^0 events in a kinematic region where the π^0 decay photons were separated by more than 3 cm were used to set this relative energy scale in order to minimize the sensitivity to possible problems in energy sharing between the photons.

An additional correction, which had to be applied separately to single photons and π^0's, arose from energy

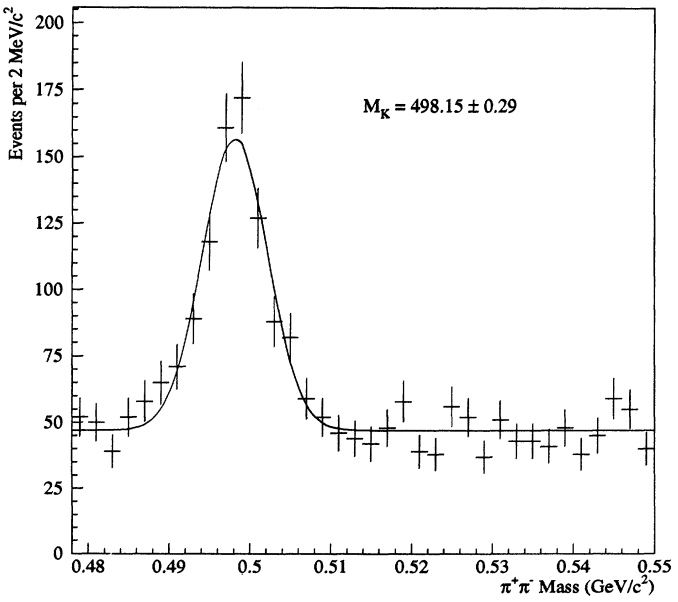

FIG. 9. $\pi^+\pi^-$ invariant mass in the K_S^0 mass region for secondary vertices upstream of the analysis magnet.

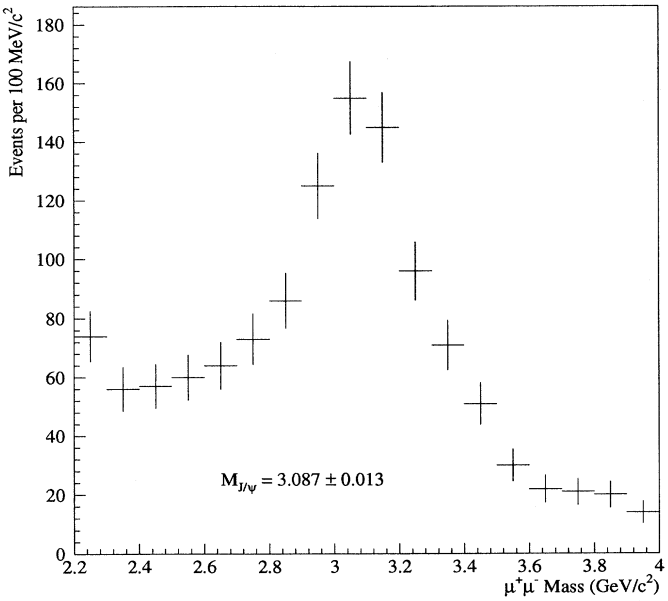

FIG. 10. $\mu^+\mu^-$ invariant mass in the J/ψ region. The J/ψ's were selected by the E672 dimuon trigger and identified by the muon spectrometer. The μ^+ and μ^- momenta were determined independent of the muon spectrometer.

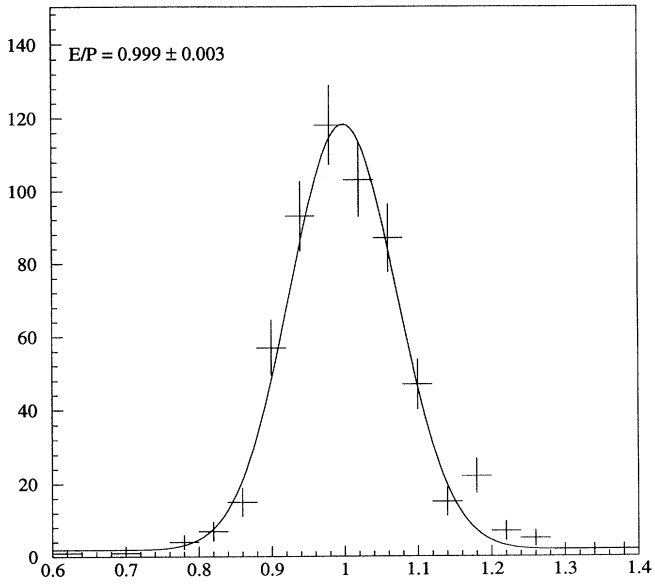

FIG. 11. Ratio of the energy reconstructed in the electromagnetic calorimeter over the momentum reconstructed using the tracking system for electrons from $\pi^0 \rightarrow \gamma e^+e^-$ decays. The plot is made using all energy corrections.

losses at the inner-outer Φ boundary. This was calculated from Monte Carlo events generated within ± 10 cm of this boundary and provided an empirical correction for the average reconstructed energy loss as a function of reconstructed energy and distance to the boundary.

The Monte Carlo simulation was also used to generate a correction for energy lost due to showering in the material in front of the active region of the electromagnetic calorimeter. This correction was determined independently for photons and electrons, as a function of energy, and applied to reconstructed showers.

The final correction to the reconstructed shower energy was determined via electrons from π^0 decay in which one photon converted into an e^+e^- pair. The ratio of the energy determined using the electromagnetic calorimeter (E) to the momentum determined by the tracking system (P) was obtained as a function of electron energy. An empirical correction to E was then calculated from the requirement that $E/P = 1.0$ for all energies. Figure 11 shows this corrected E/P distribution, and its average value, after making all adjustments. A similar correction was applied to photons scaled by the relative photon to electron energy loss in the material in front of the active region of the electromagnetic calorimeter.

The resultant π^0 mass for the three-particle γe^+e^- system is shown in Fig. 12 as a function of photon energy. The photon energy used in the calculation of the mass has all the final corrections while the e^- and e^+ momenta have the final corrections for the momentum scale of the tracking system. The agreement with the accepted value of the π^0 mass is better than 0.5%.

A correction was also applied to the π^0 energy to account for energy losses in reconstruction that depended on the spatial separation of the two decay photons in the EMLAC. These corrections were determined from Monte Carlo studies of π^0 decays, which indicated that the electromagnetic reconstruction algorithm underestimated π^0 energies for cases of highly overlapping showers. This contributed a systematic uncertainty in the π^0 cross section of less than 1%.

Using all the above corrections the π^0 and η masses in the $\gamma\gamma$ decay modes were found to be $135.26 \pm 0.06\,\mathrm{MeV}/c^2$ and $545.06 \pm 1.38\,\mathrm{MeV}/c^2$, respectively, both within 0.5% of their accepted values. The difference between the reconstructed π^0 and η masses and their accepted values, combined with the uncertainty in the γe^+e^- mass for the π^0 ($\approx 0.5\%$), and the uncertainty in the momentum scale for the tracking system ($\approx 0.5\%$), results in a systematic uncertainty in the overall energy scale of $\approx 0.9\%$, which contributes $\approx 10\%$ uncertainty to the absolute π^0 and direct-photon cross sections. Figure 13 shows the invariant $\pi^0\gamma$ mass in the ω mass range

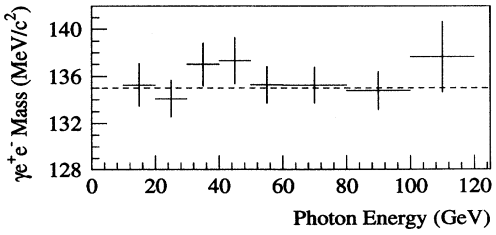

FIG. 12. Mean value of the π^0 mass for events in which one of the decay photons converted. The mean value of the reconstructed γe^-e^+ mass is plotted vs the γ energy. The mass was determined using the tracking momentum for the e^- and e^+ pairs and the LAC energy for the γ. All energies are based on the final energy scale.

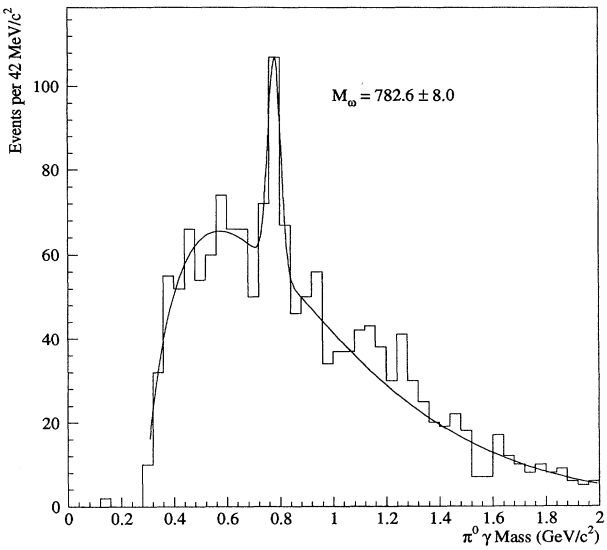

FIG. 13. $\pi^0\gamma$ invariant mass in the ω mass region. The agreement of the mass with the accepted value indicates a consistent energy scale between π^0's and photons has been established. Events selected via the LOCAL*GLOBAL trigger contribute to this plot.

which provides an independent check on our energy scale. The value of $782.6 \pm 8.0\,\mathrm{MeV}/c^2$ for the ω signal confirms the establishment of a consistent energy scale between the reconstructed π^0's and single photons. This consistency is particularly important because π^0 mesons provide the main background to the direct-photon signal, and must be properly accounted for to obtain the cross section for direct-photon production.

The contribution to the systematic uncertainty in the cross section from inaccuracies in the E/P function was estimated as follows. The normalization of the function was determined using electron calibration runs at 25, 50, and $100\,\mathrm{GeV}/c$. By varying these electron energies within their beam uncertainties (and thus the overall normalization of the E/P response function) and varying the magnitude of the relative γ/e^- energy loss function given by the Monte Carlo simulation, an estimate of the uncertainty in the cross section was obtained. The result was a contribution to the systematic uncertainty in the γ cross section of 12% and 4% in the π^0 cross section.

D. Monte Carlo simulation

The relatively small cross section for direct-photon production makes its measurement particularly sensitive to backgrounds from decays of hadrons which yield photons in the final state. The largest of these backgrounds arise from geometrical losses due to the acceptance of the EMLAC, failure to reconstruct low-energy photons from asymmetric π^0 or η decays, and coalescence of nearby photons from symmetric decays of high-energy π^0's. Such sources provide single-photon background at a level that must be estimated by Monte Carlo simulation.

The Monte Carlo simulation of the spectrometer used the GEANT [16] package developed at CERN, which contains a data base of standard geometrical shapes and material properties that can be used to model a specific detector. All the essential physics processes that take place in the development of electromagnetic showers are represented in the standard program.

An empirical parametrization was developed to simulate the deposition of the incident γ or electron energy in the appropriate strips of the EMLAC. A parametrized shower simulation was chosen because of the large CPU time required to generate complete electromagnetic showers. The parameters used in the simulation were established by a comparison of data with the full-shower Monte Carlo simulation, and were tuned by varying the input shower shape and parameters describing detector characteristics (such as the zero-suppression window and energy resolution). Test criteria were established to compare events generated by the Monte Carlo simulation with data events. After tuning the parameters, good agreement was achieved between the simulated events and the data, and the resultant Monte Carlo simulation was then used to assess backgrounds to the direct-photon signal. Each of these aspects of the overall simulation process is described below in more detail.

Simulation of detector response. The parameters for electromagnetic-shower generation were determined from 5000 75-GeV electron showers generated using the GEANT full-shower capability. The lateral shape of these showers was parametrized by a sum of three exponential terms, separately for the front and back sections of the EMLAC. The parametrized shape agreed very well with data for 50-GeV and 100-GeV electrons obtained during calibration runs, and was therefore used in high-statistics simulations of the detector response. The distribution of the ratio of energy deposited in the front of the calorimeter to that deposited in the entire calorimeter (E_f/E_t) was also determined from the full-shower GEANT study. These values of E_f/E_t were low by $\approx 3\%$ relative to those found using electron beams and were therefore raised by this amount to provide better agreement. This correction did not exhibit any energy dependence and was employed in the parametrized-shower simulations to adjust the front to total energy ratio of individual showers.

Using the parametrized shower shapes, the energies in individual calorimeter channels were then adjusted to incorporate the following additional effects. Strip energies were modified assuming a fractional energy resolution due to sampling fluctuations in the EMLAC of $16\%/\sqrt{E}$. Amplifier noise was approximated by a Gaussian distribution with a standard deviation of 83 MeV. Amplifier and analog-to-digital converter (ADC) gains were varied assuming both had standard deviations of 0.75%. The effect of the zero-suppression window used during data acquisition, the measured pedestal variations, and the presence of inactive channels in the calorimeter electronics were also included in the simulation. Finally, channel energies were modified to include a small amount of cross talk ($< 2\%$) on the low-impedance cables connecting the detector strips to their amplifier channels.

Event simulation. The Monte Carlo simulation used to calculate the background to the direct-photon signal

was based on particle distributions taken from data. This procedure did not require the use of a full event simulator, and avoided investing large amounts of CPU time generating events which were not important sources of background.

The data events in which two photons had an effective mass of $< 175\,\mathrm{MeV}/c^2$ and a $p_T > 3.0\,\mathrm{GeV}/c$ were used as the Monte Carlo input events. For each such event, the momenta of all observed photons were included in the Monte Carlo simulation, with the exception that two-photon combinations with mass $< 175\,\mathrm{MeV}/c^2$ were not treated as individual photons, but rather as π^0's, with a mass value of $135\,\mathrm{MeV}/c^2$. For each event, five Monte Carlo equivalents were generated by simultaneously rotating the original momenta of all particles by a random angle around the beam direction, and then allowing the π^0's to decay randomly in their rest frames.

To simulate background contributions from η, η', and ω decays we assumed the same production characteristics for these mesons as for π^0's, so the simulated π^0's in the Monte Carlo sample were therefore simply replaced by particles of the appropriate mass, leaving the remainder of the event kinematics unchanged. The assumption of similar production properties for the η and π^0 is consistent with our data on relative η/π^0 yields, which as we shall shortly see, do not appear to depend on p_T. The production of η' and ω mesons at high energies is not as well understood. Measurements [17] indicate that the production characteristics of these mesons are similar to that of π^0's. Although these measurements have large uncertainties, they are consistent with our assumptions, and the η' and ω mesons in aggregate represent a small fraction ($\approx 3\%$) of our direct-photon background.

In order to increase statistics at the highest-p_T values, events were also generated with the original event structure, but with leading particles ($\pi^0, \eta, \ldots$, that had initial $p_T > 4.0\,\mathrm{GeV}/c$) boosted in p_T by an additional $1.25\,\mathrm{GeV}/c$. The background attributed to the boosted samples yielded a result consistent with the original sample in the region of overlap.

To account for the systematic loss of low-energy showers (a consequence of energy loss in the material in front of the active region of the calorimeter and also the zero suppression employed in the LAC readout), low-energy photons from PYTHIA [18] generated π^0 events were added to the event driven Monte Carlo simulation in order to duplicate the particle and energy distributions observed in the data.

Acceptance and reconstruction efficiency. Geometric acceptance and reconstruction efficiencies were determined using the sample of Monte Carlo events described above. Except for the geometric acceptance calculation, kinematic regions with large inefficiencies were excluded from consideration for both Monte Carlo and real events. In particular, regions of the detector near quadrant boundaries (which abutted steel support plates), regions near the central beam hole and at the outer radius of the EMLAC, and regions between octants were not included.

The geometric acceptance for π^0's and γ's was determined as a function of p_T and rapidity. The ratio of the number of single photons, or two-photon pairs in the case of π^0 decay, found within the fiducial region to the number that were generated was determined as a function of p_T and $y_{\mathrm{c.m.}}$, using a grid of 0.1 units for $y_{\mathrm{c.m.}}$ and $0.5\,\mathrm{GeV}/c$ for p_T. To determine the acceptance at any given p_T and $y_{\mathrm{c.m.}}$, a quadratic interpolation was performed on this grid. The inverse of this acceptance ratio was used to weight single photons and π^0's in the data. The reconstruction efficiency for single photons and π^0's was determined in a similar manner using the same reconstruction algorithm employed to analyze the data. Figure 14 shows the average weight for the combined acceptance and reconstruction corrections for π^0's. The single-photon weights were essentially independent of p_T and $y_{\mathrm{c.m.}}$, with an average value of about 1.25. The π^0's had considerably larger average weights, which reflect the larger challenge of reconstructing π^0's from two photons, and the fact that to reconstruct a π^0 both photons had to fall within the acceptance of the EMLAC.

Comparison of data and Monte Carlo simulation. To verify that the Monte Carlo simulations agree with the data, a set of criteria were used to compare the results of the Monte Carlo simulation with data; these are discussed below.

Partially reconstructed or misidentified π^0's account for about 80% of the total direct-photon background. An indication of the loss of π^0's can be obtained from the two-photon energy asymmetry distribution. Figure 15 shows the background-subtracted asymmetry plot for both Monte Carlo simulation and data. The fall-off at large asymmetry values is attributed to losses of low-energy photons. The agreement between Monte Carlo simulation and data indicates that the π^0 loss is properly simulated, and that this dominant source of background to the direct-photon signal can be adequately corrected on the basis of the Monte Carlo calculation.

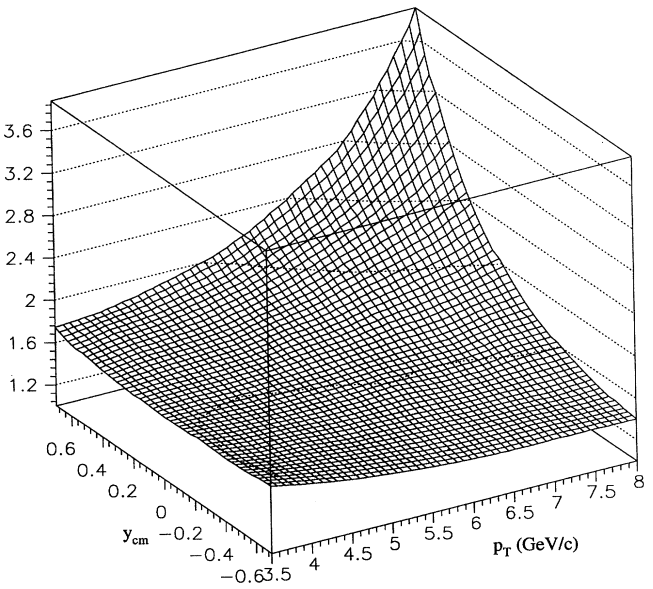

FIG. 14. Weight for acceptance and reconstruction efficiency as a function of p_T and rapidity for π^0's.

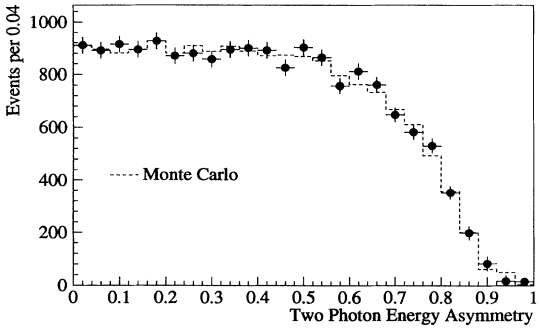

FIG. 15. The background subtracted two-photon energy asymmetry (A) distribution for photon pairs in the π^0 mass range. The Monte Carlo distribution is shown as the histogram (dashed line). The data and Monte Carlo simulation have been normalized to the same number of events. The agreement between the two distributions indicates that the Monte Carlo program is simulating the π^0 losses correctly.

Another important comparison involves the ratio of reconstructed energy in the front of the EMLAC relative to the total (E_f/E_t). Although, the value of E_f/E_t does not make a direct contribution to the direct-photon background, shifts in (E_f/E_t) can influence the reconstruction of photons and thereby the identification of π^0's or other neutral mesons. Figure 16 shows the reconstructed (E_f/E_t) ratio from Monte Carlo simulation and data for different photon energies. The agreement is relatively good over a wide range of energies, with a significant discrepancy only at the lowest energies.

Another indication of the performance of the Monte Carlo simulation is the comparison of χ^2 distributions for fitting photons to the assumed shower shapes. A systematic difference in χ^2 distributions for data and Monte Carlo simulation could imply a possible difference in the reconstruction efficiency between the two. Figure 17 shows the χ^2 distributions for reconstructed photons from Monte Carlo simulation and data. The background calculations are insensitive to small differences between these distributions. The observed level of agreement between the two distributions suggests that there are no major differences in reconstruction between data and Monte Carlo simulation.

Another measure is provided by the comparison of the two-photon invariant-mass distribution. This is plotted in Fig. 18. These distributions are also in good agreement, indicating that the Monte Carlo simulation properly represents the background photons (which contribute to the combinatorial background in the plot). The small difference observed in the tails of the π^0 peak is attributed to non-Gaussian contributions in the data that were not simulated in the Monte Carlo program. This difference was compensated for by a 2.6% correction to the π^0 cross section.

Background to the direct-photon signal. To determine the number of background single photons that satisfied the direct-photon criteria, the Monte Carlo events (which contain no direct photons) were processed using the same

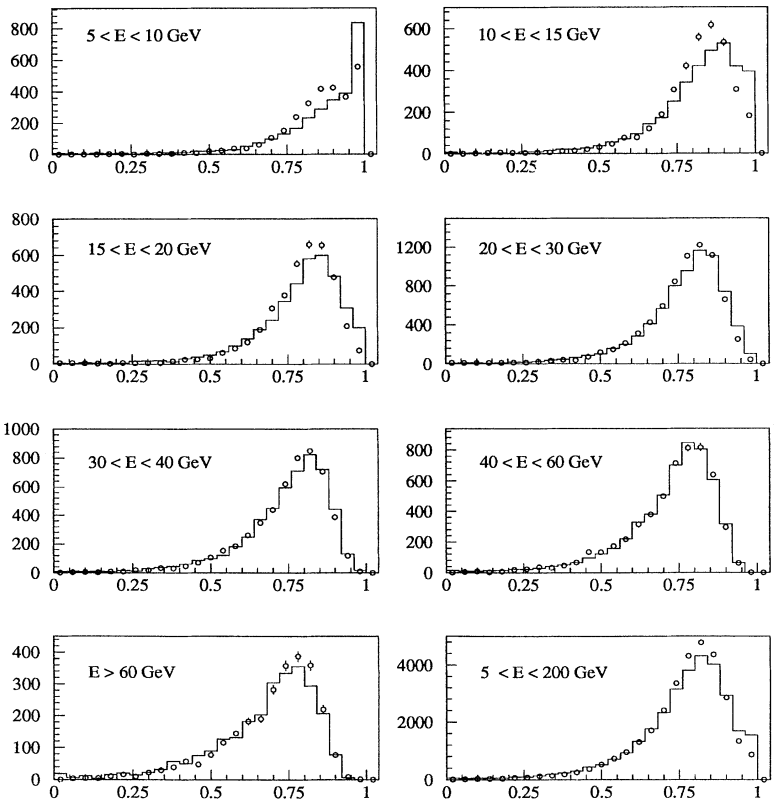

FIG. 16. Ratio of the energy deposited in the front section of the EMLAC to the total energy deposited for Monte Carlo simulation (circles) and data (histogram). The relative agreement over a wide range of photon energies (E) indicates the Monte Carlo energy deposition is similar to data. The data and Monte Carlo simulation have been normalized to the same number of events.

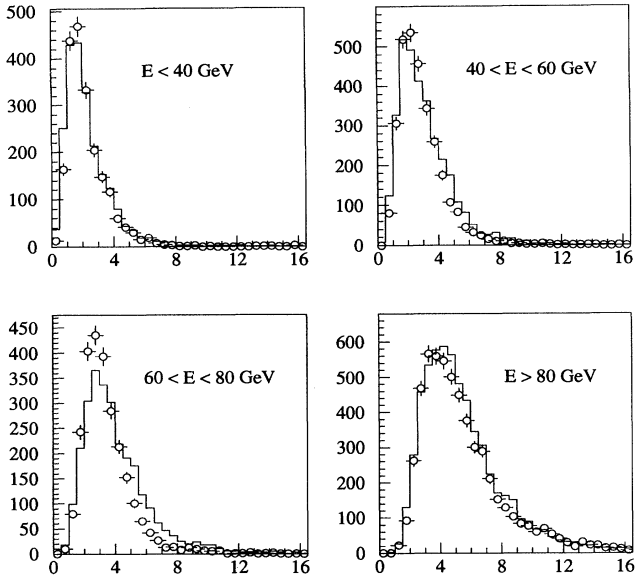

FIG. 17. $\chi^2_{\rm NDF}$ distributions for Monte Carlo showers (circles) and data showers (histogram). The agreement over a wide range in photon energies illustrates the consistency between Monte Carlo simulation and data. The data and Monte Carlo simulation have been normalized to the same number of events.

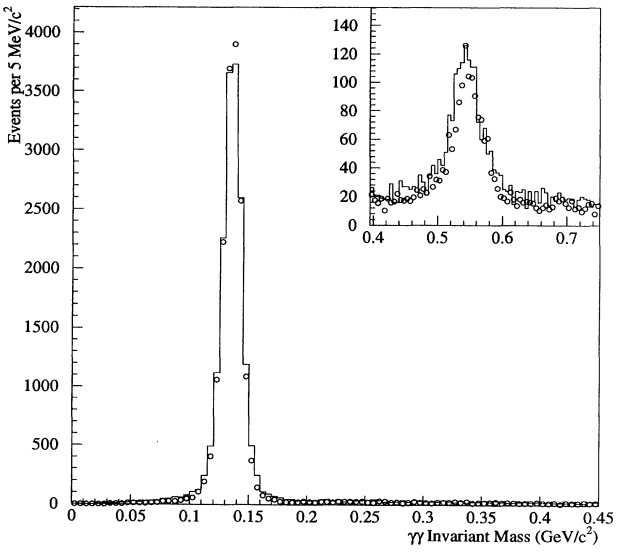

FIG. 18. The two-photon invariant mass distributions for Monte Carlo simulation (circles) and data (histogram). The agreement over the entire mass range indicates the background in the Monte Carlo simulation represents that seen in the data. The small disagreement in the π^0 mass tails indicates non-Gaussian resolution effects in the data. The data and Monte Carlo simulation have been normalized to the same number of events.

analysis code employed for analyzing the data. The reconstructed single photons and the accepted π^0 yield were then obtained as a function of p_T for four rapidity intervals: $-0.7 < y_{\rm c.m.} < 0.7$, $-0.7 < y_{\rm c.m.} < -0.2$, $-0.2 < y_{\rm c.m.} < 0.2$, and $0.2 < y_{\rm c.m.} < 0.7$. The ratio of the simulated single-photon background to the accepted π^0 signal, referred to as $(\gamma/\pi)_{\rm bck}$, was used to estimate the background contribution to the direct-photon signal in the data.

Small contributions to the background from $K^0_S \rightarrow \pi^0\pi^0$ decays, and from η decays other than the $\gamma\gamma$ mode, were estimated in a manner similar to the one described above for obtaining the backgrounds from the dominant π^0, η, and ω decays. For the relative production rates in the Monte Carlo simulation, we used $\eta/\pi^0 = 0.45$ and assumed the same value for η'/π^0, ω/π^0, and K^0_S/π^0 [17, 1]. Other contributions, e.g., from $\eta' \rightarrow \rho\gamma$, K_L decays and interactions, and neutron interactions, were found to be completely negligible in Monte Carlo studies.

Contributions to the systematic uncertainty in the estimated $(\gamma/\pi^0)_{\rm bck}$ ratio originate from the following sources:

(i) Uncertainty on the η/π^0 production ratio.

(ii) Independent uncertainties in the γ and π^0 cross sections, due to differing corrections for timing, directionality, and charged track cuts for the photon cross section, and the mass tail correction for the π^0 cross section.

(iii) An uncertainty due to the requirement that a direct-photon candidate not form a π^0 with an asymmetry of less than 0.75. This asymmetry requirement was varied between 0 and 1, and the cross sections recalculated to determine the variation of the resultant direct-photon cross section.

(iv) Uncertainties arising from the energy scale uncertainty as inferred from the small residual difference in the π^0 and η masses relative to their accepted values. This was estimated by recalculating the background using a shift in the π^0 energy scale as needed to obtain the correct π^0 mass while keeping the energy of the single-photon candidates unchanged.

(v) Uncertainties arising from the polynomial fit to the background. These uncertainties were estimated point by point using the covariance matrix of the fit.

(vi) An additional contribution to the uncertainty in the $(\gamma/\pi^0)_{\rm bck}$ arose from uncertainties in the implementation of detector effects in the Monte Carlo simulation. Effects such as energy resolution, amplifier gains, amplifier cross talk, and zero suppression, were varied within their uncertainties to gauge their impact on the estimated background.

The net result was a systematic uncertainty in the direct-photon cross section of 16% at a p_T of $4\,{\rm GeV}/c$, decreasing to 8% at a p_T of $8\,{\rm GeV}/c$.

p_T resolution. The final correction to the data accounted for the energy resolution of the detector. Since the cross section has a very steep dependence on p_T, the net effect of the p_T resolution is to shift the observed cross section from low to higher values in p_T. The resulting correction, as a function of p_T, was determined by generating direct photons and π^0's according to the p_T distributions observed in the data. The energies of the

generated photons were then smeared by the detector resolution. The ratios of the final and initial p_T distributions were then parametrized and used to correct the respective p_T spectra. The magnitude of the correction varied from about 15% in low p_T and backward rapidity regions, to about 2% at high p_T and forward rapidity, for both π^0's and direct photons. The systematic uncertainty due to this correction was $\approx 2\%$ for both the γ and π^0 cross sections.

E. Trigger corrections

Trigger corrections were calculated on an event-by-event basis using the measured trigger efficiency of the detector. The reconstructed photons in each event were used in the calculation of the trigger corrections. The reconstructed energies were first distributed into detector channels using the shower shape employed in photon reconstruction. The energies in the individual channels were then summed into groups in a manner simulating the on-line trigger. (The p_T of a group was calculated based on its radial position in the detector.) The probability that the event satisfied a trigger was then calculated using the corresponding trigger efficiency function. A representative trigger efficiency function is shown in Fig. 19. The smallest value of p_T accepted for any given trigger setting corresponded to an average trigger efficiency of $> 50\%$.

This method for determining trigger corrections is more appropriate than using a purely Monte Carlo method, because these corrections are based on the structure of individual events rather than on averages over many events. However, for unusual decay configurations this procedure can occasionally lead to large event weights. Such situations were handled by using the magnitude of the individual event-based trigger correction

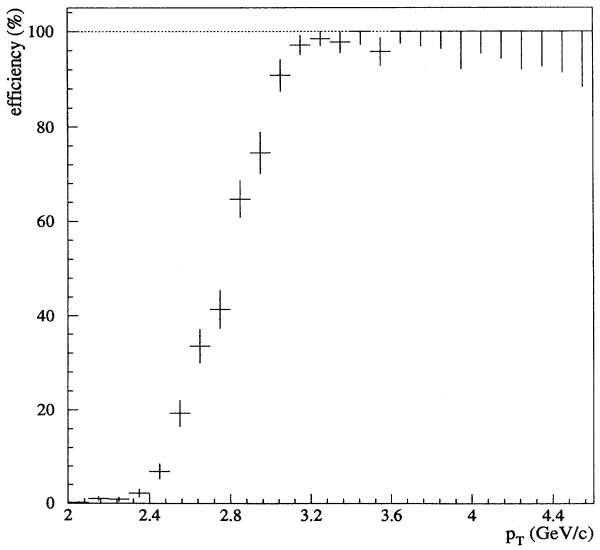

FIG. 19. An example of a trigger efficiency curve. Note the trigger efficiency rises by 50% over a transverse momentum range of $\approx 0.5\,\mathrm{GeV}/c$.

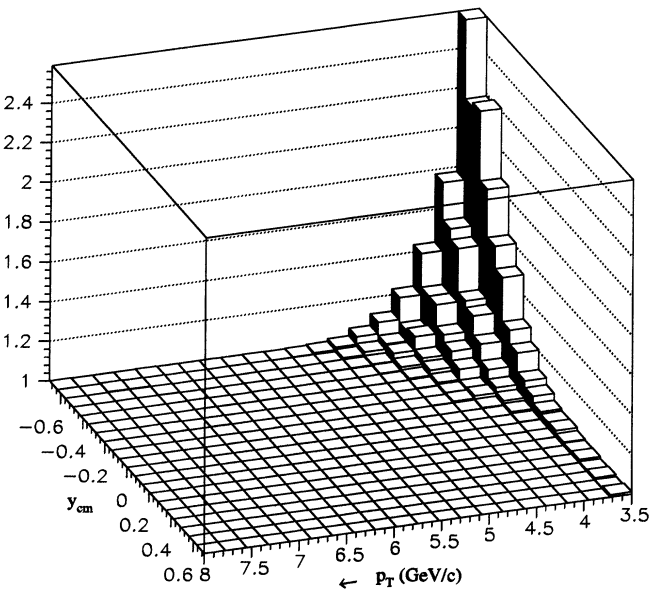

FIG. 20. Average value of the trigger corrections applied to reconstructed π^0's as a function of p_T and $y_{\mathrm{c.m.}}$.

only when it was less than 2, but using a calculated average value (determined by implementing the trigger in the Monte Carlo simulation) for events with trigger corrections that exceeded this limit. The average correction as a function of p_T and rapidity is shown in Figs. 20 and 21 for π^0 and single photons, respectively.

When the p_T observed in an event exceeded the minimum required for analysis of this trigger for any given region of the detector, a preliminary weight was calculated, as described in the previous paragraph. An additional weight is then calculated to account for any variations in the trigger performance of other octants by determining whether the event would have satisfied the trigger in the

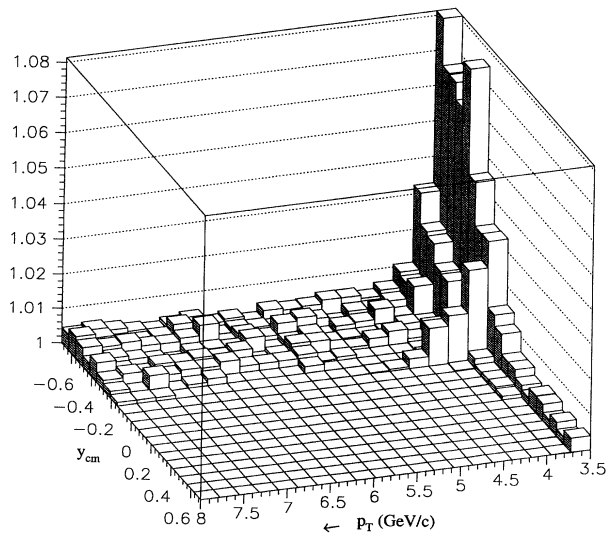

FIG. 21. Average value of the trigger corrections applied to reconstructed single photons as a function of p_T and $y_{\mathrm{c.m.}}$.

TABLE I. Average value of some corrections applied to the data. All corrections are listed for data taken with the Be target.

Correction for	$\pi^-\text{Be} \to \pi^0 X$	$p\text{Be} \to \pi^0 X$	$\pi^-\text{Be} \to \gamma X$	$p\text{Be} \to \gamma X$
Beam absorption	1.051	1.069	1.051	1.069
Vertex reconstruction	1.065	1.065	1.065	1.065
Veto wall backscatter	1.030	1.035	1.030	1.035
No veto wall hit requirement	1.085	1.085	1.085	1.085
Uncorrelated energy	1.005	1.008	1.005	1.008
γ conversion	1.148	1.147	1.071	1.071
δ_r	-	-	1.005	1.007
Timing	-	-	1.027	1.028
E_f/E_t cut	-	-	1.015	1.015
Tracking	-	-	1.006	1.006
Direct photons making a π^0 or η combination	-	-	1.101	1.105
Resolution in p_T	0.922	0.909	0.971	0.943

TABLE II. Compilation of the major systematic uncertainties for inclusive π^0 and direct-photon cross sections.

Source of uncertainty	$\pi^-\text{Be} \to \pi^0 X$	$p\text{Be} \to \pi^0 X$	$\pi^-\text{Be} \to \gamma X$	$p\text{Be} \to \gamma X$
E/P function	4%	4%	12%	12%
Trigger	1.5% $\to <$ 0.1%	3.5% $\to <$ 0.1%	5.5% $\to <$ 0.1%	12.0% $\to <$ 0.1%
$(\gamma/\pi^0)_{\text{bck}}$ subtraction	-	-	16% $\to$ 8%	16% $\to$ 8%
Normalization	10%	10%	10%	10%

TABLE III. Invariant differential cross section $\left(d\sigma/\pi\, dp_T^2 dy_{\text{c.m.}}\right)$ for the inclusive reaction $\pi^- + \text{Be} \to \pi^0 + X$. Cross sections are per nucleon in units of pb/(GeV/c)^2. The first uncertainty is statistical while the second is systematic.

p_T (GeV/c)	$-0.7 < y_{\text{c.m.}} < -0.2$	$-0.2 < y_{\text{c.m.}} < 0.2$	$0.2 < y_{\text{c.m.}} < 0.7$
3.5 – 3.75	16500 ± 800 ± 3000	19000 ± 700 ± 2200	19800 ± 600 ± 2100
3.75 – 4.0	8200 ± 400 ± 1100	8700 ± 400 ± 1000	9600 ± 400 ± 1000
4.0 – 4.25	3770 ± 200 ± 530	4760 ± 190 ± 550	4670 ± 160 ± 500
4.25 – 4.5	1970 ± 120 ± 260	2510 ± 140 ± 290	2550 ± 110 ± 280
4.5 – 4.75	972 ± 77 ± 140	1190 ± 71 ± 140	1110 ± 60 ± 120
4.75 – 5.0	572 ± 45 ± 75	703 ± 51 ± 81	730 ± 48 ± 79
5.0 – 5.5	255 ± 19 ± 33	302 ± 22 ± 35	298 ± 20 ± 33
5.5 – 6.0	72.5 ± 9.3 ± 9.3	85.7 ± 11.3 ± 9.9	101 ± 11 ± 11
6.0 – 7.0	10.9 ± 2.3 ± 1.4	16.8 ± 3.3 ± 1.9	11.9 ± 2.7 ± 1.3
7.0 – 8.0	0.6 ± 0.6 ± 0.1	1.4 ± 0.8 ± 0.2	3.3 ± 1.3 ± 0.4
8.0 – 10.0	0.13 ± 0.13 ± 0.02	0.25 ± 0.35 ± 0.03	0.23 ± 0.23 ± 0.03

TABLE IV. Invariant differential cross section $\left(d\sigma/\pi\, dp_T^2 dy_{\text{c.m.}}\right)$ for the inclusive reaction $p + \text{Be} \to \pi^0 + X$. Cross sections are per nucleon in units of pb/(GeV/c)^2.

p_T (GeV/c)	$-0.7 < y_{\text{c.m.}} < -0.2$	$-0.2 < y_{\text{c.m.}} < 0.2$	$0.2 < y_{\text{c.m.}} < 0.7$
4.0 – 4.25	3640 ± 180 ± 650	4050 ± 160 ± 470	3020 ± 110 ± 330
4.25 – 4.5	1800 ± 100 ± 250	2130 ± 110 ± 250	1790 ± 83 ± 190
4.5 – 4.75	879 ± 58 ± 123	1040 ± 55 ± 120	859 ± 46 ± 94
4.75 – 5.0	446 ± 33 ± 58	503 ± 36 ± 58	374 ± 29 ± 41
5.0 – 5.5	197 ± 14 ± 25	237 ± 17 ± 27	159 ± 12 ± 17
5.5 – 6.0	44.7 ± 5.9 ± 5.7	69 ± 8 ± 8	41.3 ± 6.2 ± 4.5
6.0 – 7.0	6.9 ± 1.7 ± 0.9	8.5 ± 2.2 ± 1.0	11.0 ± 2.0 ± 1.2
7.0 – 8.0	0.22 ± 0.22 ± 0.02	0.95 ± 0.55 ± 0.11	–

other octants as well. This weight accounts for threshold variations and dead channels in other octants. We thus corrected automatically for trigger variations at fixed rapidity for all octants.

The systematic uncertainty introduced by the trigger corrections was estimated in two ways. The first method involved comparing π^0 cross sections from runs with different trigger thresholds; the cross section in the turn-on region for the run with the higher trigger threshold was compared to the cross section for the run with the lower trigger threshold which was nearly 100% efficient in this region. The second method involved shifting the trigger turn on curve for a given run by one standard deviation to determine the sensitivity of the cross section to the threshold measurement. Comparing runs with different trigger thresholds indicated an uncertainty of 2.5% at a p_T corresponding to a trigger efficiency of 80%. The p_T dependence of this systematic uncertainty was parametrized using a function whose shape was determined by the p_T dependence of the average trigger corrections, normalized to 2.5% at the p_T corresponding to a trigger efficiency of 80%. Although, the second technique yielded much lower estimates of these systematic uncertainties, the uncertainties estimated through the first procedure were used as upper limits to the actual uncertainties from the trigger.

Because of the inefficiencies in the pretrigger, an additional p_T independent correction of 17% for the backward rapidity region and 2% for the central and forward rapidity regions was applied to each cross section, which contributed an additional systematic uncertainty of 2%.

F. Other corrections to the cross sections

In addition to the corrections discussed in the preceding sections, the reported invariant cross sections also include corrections for the following effects:

(i) Absorption of beam particles. This correction was calculated based on the material between the beam counters and the interaction point in the target. The average correction was 6%.

(ii) Vertex reconstruction inefficiency. This correction was determined from a visual examination of events that did not have a reconstructed vertex. The correction was found to be linear in vertex position, decreasing from 1.09 at the upstream end of the target, to 1.04 at the downstream end, with an average correction of 6.5%.

(iii) On-line veto due to backscatter. Corrections were made for losses of events in which particles from the interaction were emitted backward into the veto walls, thereby vetoing the event. The magnitude of this correction de-

TABLE V. Invariant differential cross section $(d\sigma/\pi\, dp_T^2 dy_{\text{c.m.}})$ for the inclusive reactions $\pi^- + \text{Be} \to \pi^0 + X$ and $p + \text{Be} \to \pi^0 + X$ averaged over the full rapidity range $-0.7 < y_{\text{c.m.}} < 0.7$. Cross sections are per nucleon in units of $\text{pb}/(\text{GeV}/c)^2$.

p_T (GeV/c)	$\pi^- + \text{Be} \to \pi^0 + X$	$p + \text{Be} \to \pi^0 + X$
3.5 – 3.75	$18400 \pm 400 \pm 2200$	–
3.75 – 4.0	$8900 \pm 200 \pm 1000$	–
4.0 – 4.25	$4370 \pm 110 \pm 500$	$3540 \pm 90 \pm 420$
4.25 – 4.5	$2330 \pm 70 \pm 270$	$1890 \pm 60 \pm 220$
4.5 – 4.75	$1080 \pm 40 \pm 130$	$920 \pm 30 \pm 110$
4.75 – 5.0	$665 \pm 28 \pm 76$	$437 \pm 19 \pm 50$
5.0 – 5.5	$284 \pm 12 \pm 33$	$195 \pm 8 \pm 22$
5.5 – 6.0	$86.6 \pm 6.1 \pm 9.9$	$50 \pm 4 \pm 6$
6.0 – 7.0	$13.0 \pm 1.6 \pm 1.5$	$8.8 \pm 1.1 \pm 1.0$
7.0 – 8.0	$1.8 \pm 0.6 \pm 0.2$	$0.35 \pm 0.18 \pm 0.04$
8.0 – 10.0	$0.20 \pm 0.14 \pm 0.02$	$0.11 \pm 0.08 \pm 0.01$

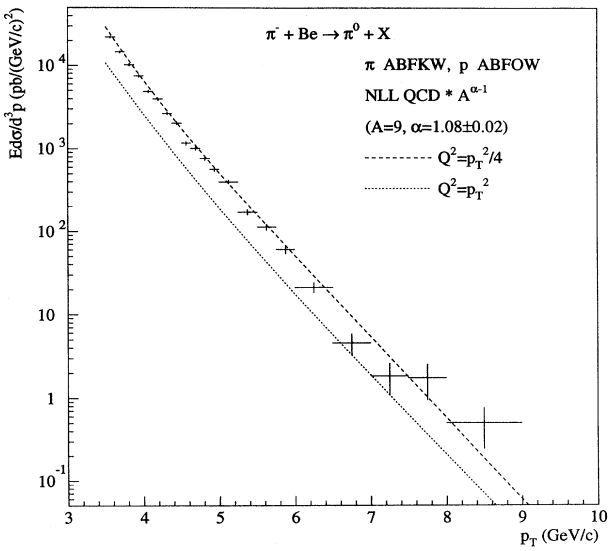

FIG. 22. Invariant cross section per nucleon for π^0 production for π^- interactions with Be. Cross sections are shown vs p_T over the full rapidity range $-0.7 < y_{\text{c.m.}} < 0.7$. The curves represent QCD calculations as described in the text.

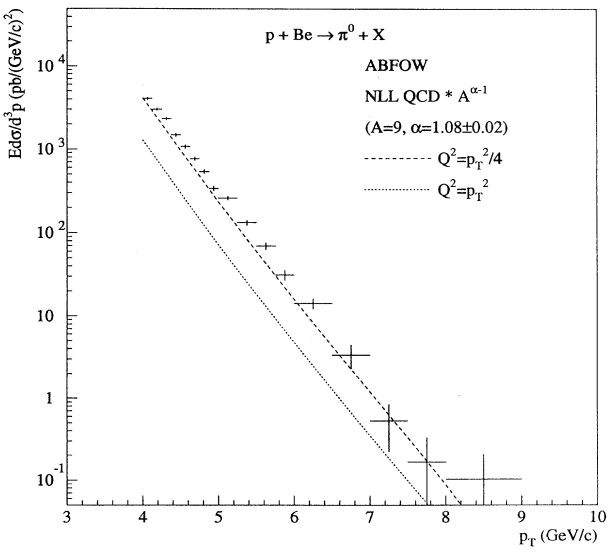

FIG. 23. Invariant cross section per nucleon for π^0 production for proton interactions with Be. Cross sections are shown vs p_T over the full rapidity range $-0.7 < y_{\text{c.m.}} < 0.7$. The curves represent QCD calculations as described in the text.

TABLE VI. Invariant differential cross section $(d\sigma/\pi\, dp_T^2 dy_{\text{c.m.}})$ for the inclusive reactions $\pi^- + \text{Cu} \to \pi^0 + X$ and $p + \text{Cu} \to \pi^0 + X$ averaged over the full rapidity range $-0.7 < y_{\text{c.m.}} < 0.7$. Cross sections are per nucleon in units of $\text{pb}/(\text{GeV}/c)^2$.

p_T (GeV/c)	$\pi^- + \text{Cu} \to \pi^0 + X$	$p + \text{Cu} \to \pi^0 + X$
3.5 – 3.75	21400 ± 1100 ± 2600	-
3.75 – 4.0	9700 ± 640 ± 1100	-
4.0 – 4.25	4800 ± 350 ± 570	4200 ± 240 ± 510
4.25 – 4.5	3110 ± 260 ± 360	2070 ± 140 ± 240
4.5 – 4.75	1470 ± 180 ± 170	990 ± 90 ± 120
4.75 – 5.0	545 ± 94 ± 64	590 ± 70 ± 70
5.0 – 5.5	291 ± 51 ± 34	206 ± 27 ± 24
5.5 – 6.0	107 ± 28 ± 12	58.7 ± 14.0 ± 6.9
6.0 – 7.0	17.1 ± 7.7 ± 2.0	13.0 ± 4.2 ± 1.5
7.0 – 8.0	1.7 ± 4.8 ± 0.2	1.6 ± 1.6 ± 0.2
8.0 – 10.0	0.79 ± 0.79 ± 0.09	1.2 ± 0.9 ± 0.1

pended on the target configuration. The correction was determined using minimum-bias events which did not include veto-wall signals in the trigger. The fraction of events in which the veto wall had a signal in time was studied as a function of the number of interaction counters that had signals. This was used to generate a correction for the number of accidentally vetoed events due to backscatter, which corresponded typically to losses of $\approx 3.5\%$. We assume that the correction for direct photon and π^0 triggers is comparable to that for minimum-bias events.

(iv) Losses due to the off-line criteria on signals in the veto wall. In order to eliminate events triggered by a muon, an event was rejected if either of the veto walls had a signal corresponding to the triggering quadrant of the EMLAC. Losses from random coincidences with good events were corrected by determining the fraction of good π^0 events that were eliminated by the application of the veto-wall criteria. This correction averaged 8.5%. The same correction was used for direct photons.

(v) Losses due to the uncorrelated energy requirement. A procedure similar to the above was used to estimate the loss of events from the requirement of having small uncorrelated energy in the trigger quadrant. This correction averaged approximately 0.6%.

(vi) Losses due to γ conversions in material downstream of the interaction vertex. The correction for photon conversions downstream of the vertex was found by

TABLE VII. Values for α averaged over the rapidity range $-0.7 < y_{\text{c.m.}} < 0.7$ for π^- and p induced collisions. α was determined assuming an A^α dependence for the cross sections on Be and Cu.

p_T (GeV/c)	α_{π^-}	α_p
3.5 – 4.0	1.06 ± 0.02	-
4.0 – 4.5	1.10 ± 0.03	1.07 ± 0.03
4.5 – 5.0	1.03 ± 0.06	1.10 ± 0.04
5.0 – 6.0	1.06 ± 0.08	1.05 ± 0.07
4.0 – 8.0	1.08 ± 0.02	1.08 ± 0.02

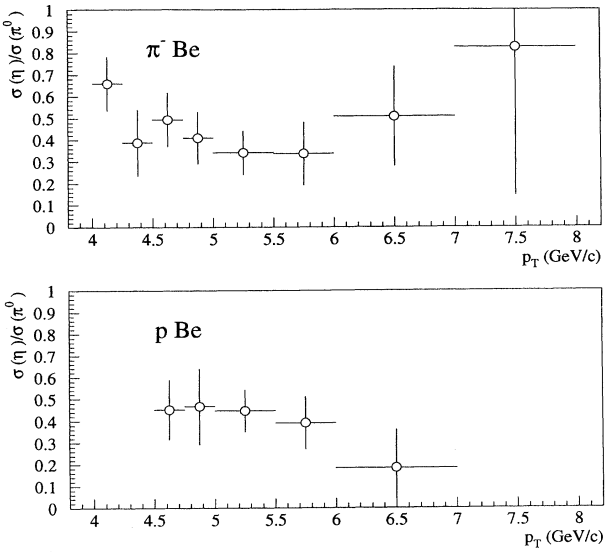

FIG. 24. Ratio of the invariant η cross section over the invariant π^0 cross section as a function of p_T.

tracking individual photon trajectories to determine the number of radiation lengths of material the photon traveled through. The average correction corresponded to 7% per photon.

(vii) Asymmetry cuts applied to π^0 and η candidates. Asymmetry cuts of 0.75 (0.6) were applied to two-photon pairs in the π^0 (η) mass regions to obtain clean samples of data for the π^0 and η cross sections. The isotropy of π^0 and η decay was used to account for these losses.

(viii) Losses due to restrictions on photon directionality, photon arrival time, E_f/E_t, and the restriction that

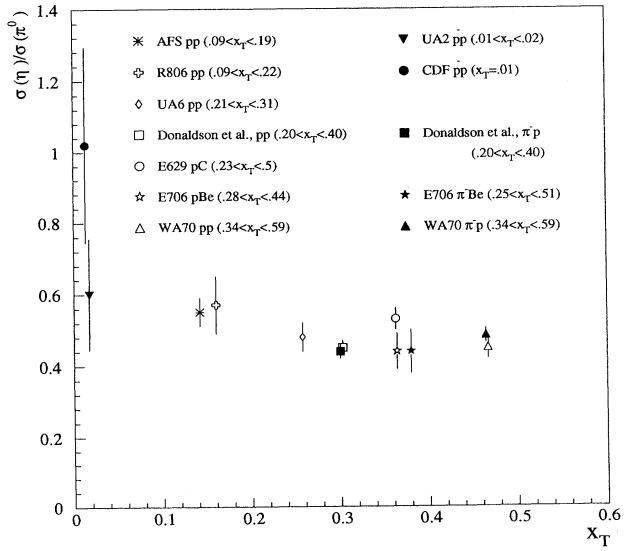

FIG. 25. Ratio of the invariant cross section for η production over π^0 cross section as a function of x_T $(= 2p_T/\sqrt{s})$ for high-p_T production experiments. The range in x_T covered by each experiment is listed and the data point is positioned at the center of this range.

charged tracks not overlap with showers. These criteria were applied to minimize background from muons and hadrons in the direct-photon signal. Only a small number of photons were removed by these cuts, for which a correction was estimated by gauging their effect on photons originating from π^0 decays. The correction was 5.5% for direct photons.

(ix) Losses of direct photons due to random combinations with other photons resulting in a pair in the π^0 or η mass band. This loss was estimated from the Monte Carlo simulation by replacing π^0's or η's in an event with single photons of the same momentum. The events were then reconstructed and the fraction of single photons that were lost was determined as a function of p_T. This dependence was used to correct the observed direct-photon signal; the correction factor was typically 10%.

Table I summarizes the corrections discussed above, for π^0 and γ cross sections, for both beam polarities, on Be. Except for the overall trigger and acceptance corrections, corrections to the η cross section are similar to those for π^0 production.

The net systematic uncertainty in the overall normalization due to the corrections listed above, as well as from several smaller effects (at the 1% level) that have not been described, is $\approx 10\%$.

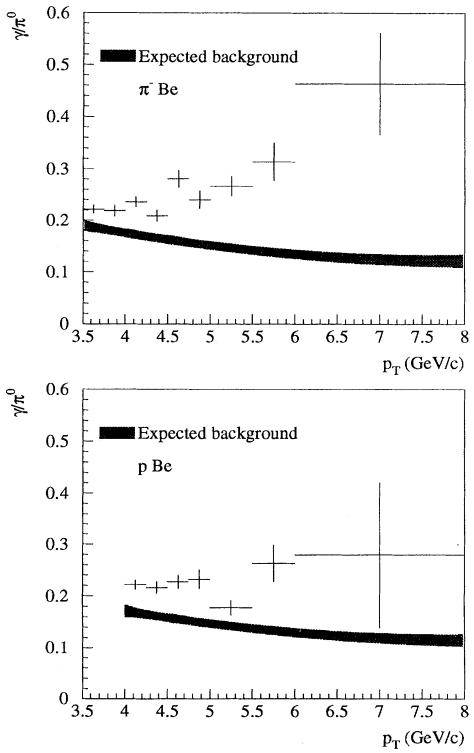

FIG. 26. The observed γ/π^0 ratios at 500 GeV/c for π^- and proton interactions with Be. The band represents Monte Carlo estimates of the contributions from meson decays including the systematic uncertainty on these estimates. The error bars on the points represent only statistical uncertainties. The ratio is averaged over the rapidity range $-0.7 < y_{\text{c.m.}} < 0.7$.

G. Summary of systematic uncertainties

The primary contributions to the systematic uncertainty arise from the following sources: uncertainty in the determination of the EMLAC energy as given by the (E/P) function, uncertainty in the magnitude of the trigger corrections, uncertainty in parameters related to background subtraction for the direct-photon cross section (including such issues as proper modeling of the detector response), and the overall normalization. These systematic uncertainties have been discussed in the preceding sections. These systematic uncertainties for the direct-photon and π^0 cross sections are summarized in Table II and, combined in quadrature, are quoted with the cross sections in the appropriate tables. Combining these systematic uncertainties yields a net uncertainty in the direct-photon cross section of $\approx 25\%$ at a p_T of 4 GeV/c, which decreases to $\approx 16\%$ at a p_T of 8 GeV/c; for the π^0 cross section the uncertainty is $\approx 11\%$ for all p_T values.

Based on the analysis of the final distribution of $\gamma\gamma$ pairs in the π^0 and η mass regions, and results from γe^+e^- studies, we estimate an upper limit on the uncertainty in the energy scale of 0.9%. This represents an uncertainty in the energy scale and contributes an additional $\approx 10\%$ uncertainty to the cross sections, which has not been included in the tables.

The central values of the beam momenta were uncertain to $\approx 2\%$. This introduces an uncertainty ($\approx 10\%$) in the calculation of the theoretical expectations.

IV. CROSS SECTIONS

A. Neutral mesons

Tables III, IV, and V show the invariant cross sections per nucleon for π^0 production in 500 GeV/c π^-Be and pBe interactions, respectively, for three regions of rapidity as well as the full rapidity range, as a function of p_T. These results are more comprehensive than those given in our previous abbreviated publication [8]. Figures 22 and 23 show the cross sections for the same data sets averaged over the rapidity range $-0.7 < y_{\text{c.m.}} < 0.7$.

The curves in Figs. 22 and 23 represent next-to-leading-log QCD calculations based upon the code provided by Aversa *et al.* [19], using parton distribution functions for the pion and nucleon from Aurenche *et al.* [20]. The calculated cross sections are illustrated for two choices of the scale ($Q^2 = p_T^2$ and $Q^2 = p_T^2/4$). Agreement between data and theory (for the smaller choice of scale) is reasonable for both the π^- and proton data over the full p_T range shown.[1]

[1]The calculations used preliminary π^0 fragmentation functions provided by J. P. Guillet *et al.* (private communication). E706 π^0 production data were included in the fragmentation fits. However, data from UA2 and the ISR dominated the determination of the gluon fragmentation function, while the quark fragmentation function was constrained primarily by results from e^+e^- data.

TABLE VIII. Invariant differential cross section $(d\sigma/\pi\, dp_T^2 dy_{\text{c.m.}})$ for the inclusive reaction $\pi^- + \text{Be} \to \gamma + X$. Cross sections are per nucleon in units of pb/(GeV/c)^2.

p_T (GeV/c)	$-0.7 < y_{\text{c.m.}} < -0.2$	$-0.2 < y_{\text{c.m.}} < 0.2$	$0.2 < y_{\text{c.m.}} < 0.7$
3.5 – 4.0	-	$690 \pm 150 \pm 160$	$647 \pm 130 \pm 190$
4.0 – 4.5	$215 \pm 43 \pm 53$	$252 \pm 45 \pm 51$	$117 \pm 35 \pm 39$
4.5 – 5.0	$83 \pm 16 \pm 17$	$126 \pm 18 \pm 23$	$83 \pm 15 \pm 19$
5.0 – 5.5	$29 \pm 8 \pm 6$	$46 \pm 9 \pm 8$	$30 \pm 8 \pm 6$
5.5 – 6.0	$12 \pm 4 \pm 2$	$22 \pm 6 \pm 4$	$13 \pm 4 \pm 3$
6.0 – 7.0	$4.2 \pm 1.3 \pm 0.8$	$5.9 \pm 1.7 \pm 1.0$	$6.5 \pm 1.5 \pm 1.2$
7.0 – 10.0	$0.38 \pm 0.18 \pm 0.07$	$0.23 \pm 0.16 \pm 0.04$	$0.18 \pm 0.15 \pm 0.03$

The analogous results for π^0 production in π^-Cu and pCu collisions, averaged over the rapidity range $-0.7 < y_{\text{c.m.}} < 0.7$, are given in Table VI as a function of p_T.

A dependence. The cross sections for π^0 and γ production are reported per nucleon. However, effects such as nuclear shadowing or secondary scattering in the nucleus can result in deviations of the cross sections from linear dependence on the nucleon number. The form A^α, with α being a parameter that can depend on rapidity, p_T and on the nature of the particle in question, is often used to parametrize the A dependence. Table VII shows the measured values of α determined for π^0 production for π^- and proton induced collisions on Cu and Be targets. The average values of α for both beams are consistent with one another and indicate a small deviation from unity. The results are consistent with previous measurements by the Chicago-Princeton group [21], as well as recent measurements from Fermilab experiment E605 [22], for similar regions of p_T. The curves shown in the Figs. 22 and 23 have been calculated using a value of α equal to 1.08.

The value of α was not well determined for direct-photon production due to inadequate statistics for data on Cu. Recent runs of E706 have a far larger sample of direct-photon events from Be, Cu, and hydrogen targets, and are expected to yield a value of α for direct-photon production.

η/π^0 production ratio. The corrections necessary to measure η production were determined using methods similar to those already described for π^0's. The measured ratio of η/π^0 production is shown in Fig. 24; within the rather large uncertainties no significant dependence on p_T or on incident beam is observed. The average value for the η/π^0 production ratio is $0.44 \pm 0.05 \pm 0.05$ for π^-Be interactions and $0.44 \pm 0.06 \pm 0.05$ for pBe interactions. Systematic uncertainties on these results are of the same magnitude as the statistical uncertainties and primarily reflect residual uncertainties in the trigger corrections and in the energy scale. Figure 25 summarizes our results and those of selected previous measurements [23]. Although our pBe result is somewhat lower than those of the ISR experiments, all the data are compatible within their statistical uncertainties.

B. Direct-photon cross sections

Figure 26 displays the observed γ/π^0 production ratio for π^-Be and pBe interactions as a function of p_T. Photons contributing to $\gamma\gamma$ pairs in the π^0 or η mass regions (with energy asymmetries less than 0.75) are excluded from the direct-photon sample; however, no isolation cuts are imposed. The bands shown in the figure represent Monte Carlo estimates of the residual contributions to these ratios from photons originating from meson decays; 80% of this background is due to π^0 decays and the rest is dominantly due to η mesons. The width of the bands represent the systematic uncertainties on the Monte Carlo calculation.

The background estimates shown in Fig. 26 are lower than those in the corresponding figures in our earlier paper [8]. Although the difference is relatively small—a shift downward of the midpoint of the band by about 30% of its width at the lowest values of p_T, and essentially no change at high p_T—the effect is systematic, and moreover the direct-photon signal, which is proportional to the difference between the data points in Fig. 26 and the estimated background, is sensitive to even such small effects. This change, which results from an overestimation of the contribution from π^0 decays in our earlier analysis, has been incorporated into the inclusive cross sections presented below, which as a result are slightly higher at the lowest values of p_T (by 60% of the estimated systematic uncertainties) than those presented in our earlier paper.

TABLE IX. Invariant differential cross section $\left(d\sigma/\pi\, dp_T^2 dy_{\text{c.m.}}\right)$ for the inclusive reaction $p + \text{Be} \to \gamma + X$. Cross sections are per nucleon in units of pb/(GeV/c)^2.

p_T (GeV/c)	$-0.7 < y_{\text{c.m.}} < -0.2$	$-0.2 < y_{\text{c.m.}} < 0.2$	$0.2 < y_{\text{c.m.}} < 0.7$
4.0 – 4.5	$134 \pm 34 \pm 50$	$161 \pm 34 \pm 38$	$139 \pm 26 \pm 33$
4.5 – 5.0	$54 \pm 12 \pm 14$	$65 \pm 12 \pm 14$	$37 \pm 10 \pm 9$
5.0 – 6.0	$6.3 \pm 2.7 \pm 1.5$	$6.6 \pm 3.1 \pm 1.8$	$7.4 \pm 2.5 \pm 1.7$
6.0 – 7.0	$0.97 \pm 0.64 \pm 0.19$	$2.4 \pm 0.9 \pm 0.5$	$0.86 \pm 0.69 \pm 0.20$

TABLE X. Invariant differential cross section ($d\sigma/\pi\, dp_T^2 dy_{\text{c.m.}}$) for the inclusive reactions $p + \text{Be} \to \gamma + X$ and $\pi^- + \text{Be} \to \gamma + X$. Cross sections are per nucleon in units of pb/(GeV/c)^2 and cover the rapidity range $-0.7 < y_{\text{c.m.}} < 0.7$.

p_T (GeV/c)	$\pi^- + \text{Be} \to \gamma + X$	$p + \text{Be} \to \gamma + X$
3.5 – 3.75	$654 \pm 140 \pm 210$	-
3.75 – 4.0	$355 \pm 88 \pm 98$	-
4.0 – 4.25	$280 \pm 39 \pm 63$	$190 \pm 30 \pm 46$
4.25 – 4.5	$101 \pm 25 \pm 25$	$103 \pm 20 \pm 23$
4.5 – 4.75	$131 \pm 16 \pm 26$	$66 \pm 11 \pm 15$
4.75 – 5.0	$58 \pm 10 \pm 11$	$36 \pm 7 \pm 8$
5.0 – 5.5	$34 \pm 5 \pm 6$	$6.8 \pm 2.7 \pm 1.9$
5.5 – 6.0	$15 \pm 3 \pm 3$	$6.5 \pm 1.6 \pm 1.3$
6.0 – 7.0	$5.5 \pm 0.9 \pm 1$	$1.32 \pm 0.43 \pm 0.25$
7.0 – 8.0	$0.46 \pm 0.24 \pm 0.08$	$0.06 \pm 0.08 \pm 0.01$
8.0 – 10.0	$0.16 \pm 0.08 \pm 0.03$	-

Tables VIII, IX, and X show the invariant cross sections per nucleon for direct-photon production in π^-Be and pBe interactions for different rapidity ranges, as a function of p_T. Figures 27 and 28 display the invariant cross section averaged over the full rapidity range of $-0.7 < y_{\text{c.m.}} < 0.7$. The curves represent next-to-leading-log QCD predictions from Aurenche *et al.* [4], using parton distribution functions [20] determined from deep inelastic scattering data and WA70 direct-photon data to constrain the gluon contribution.

The calculations shown are for $Q^2 = p_T^2$, $Q^2 = p_T^2/4$, and for Q^2 chosen through the principle of minimum sensitivity (PMS) [24]. The PMS procedure selects factorization and renormalization scales that minimize the dependence of the calculated cross section on these parameters. The Q^2 defined by the PMS technique depends on the region of phase space used in the minimization, but can be as low as $\approx 0.1\, p_T^2$. Although the scale determined by PMS is smaller than what one might intuitively expect, the PMS procedure has been successfully employed in fitting other direct-photon data [20,26]. The data tend to favor QCD predictions using a smaller choice of scale.

Figure 29 shows the ratio of direct-photon cross sections for π^-Be interactions to that for pBe interactions. The ratio of cross sections tends to minimize ambiguities that may exist in the normalization of data and the-

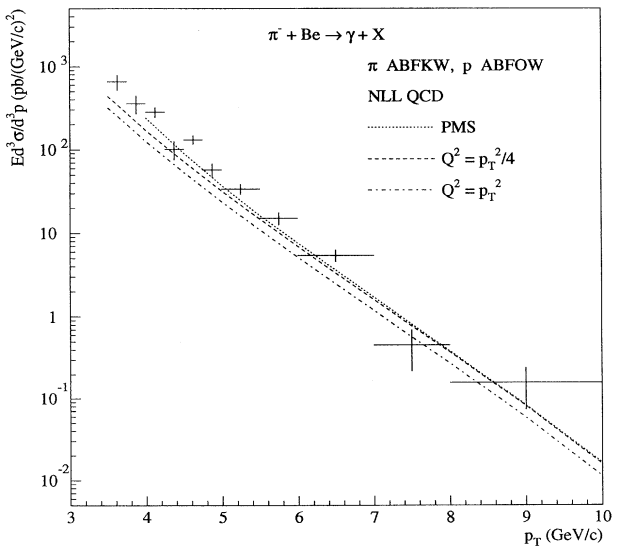

FIG. 27. Invariant differential cross section per nucleon for direct-photon production from π^- interactions with Be. Cross sections are shown vs p_T for the full rapidity range $-0.7 < y_{\text{c.m.}} < 0.7$. The curves represent QCD predictions as described in the text.

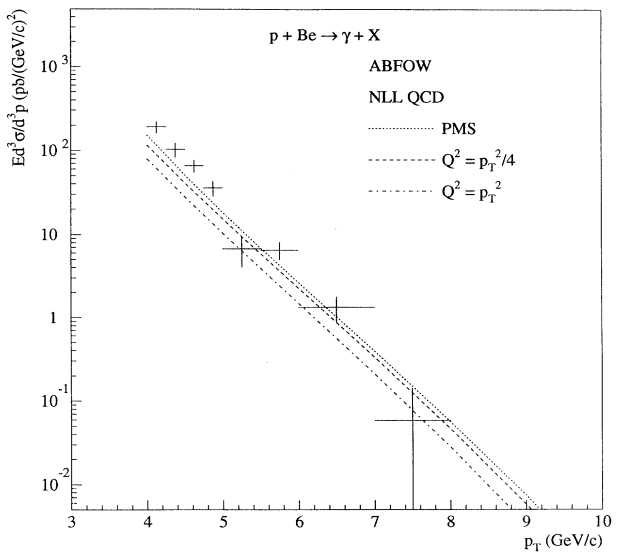

FIG. 28. Invariant differential cross section per nucleon for direct-photon production from proton interactions with Be. Cross sections are shown vs p_T over the full rapidity range $-0.7 < y_{\text{c.m.}} < 0.7$. The curves represent QCD predictions as described in the text.

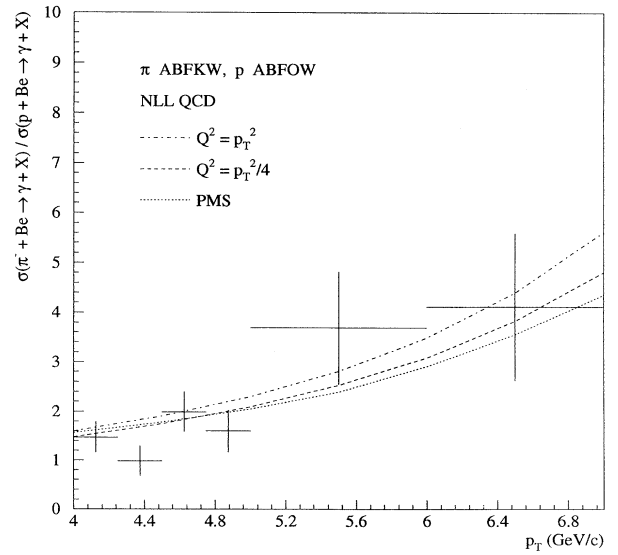

FIG. 29. Ratio of the invariant cross section for direct-photon production from π^-Be interactions and pBe interactions. The ratio is averaged over the rapidity range $-0.7 < y_{\text{c.m.}} < 0.7$.

ory. The curves again represent next-to-leading-log QCD predictions from Aurenche *et al.* [4], showing results for scales selected via PMS, $Q^2 = p_T^2/4$ and $Q^2 = p_T^2$ with the parton distribution functions of Aurenche *et al.* [20]. The agreement between QCD predictions and the ratio of cross sections is good over the entire range of p_T, independent of the definition of Q^2.

C. Comparison with theoretical expectations

The spread in the theoretical expectations of the next-to-leading-log QCD cross sections can be gauged from the differences obtained for predictions using different recent parton distribution functions. In the following comparisons we have used the nucleon parton distribution functions: Aurenche *et al.* (ABFOW) [20], Glück *et al.* (GRV) [25], Martin *et al.* (MRS) [26], Morfín and Tung (MT) [27], and the pion parton distribution functions: Aurenche *et al.* (ABFKW) [20], Glück *et al.* (GRV) [25], and Sutton *et al.* (SMRS) [28]. This selection represents current parton distribution functions that have been evaluated at the next-to-leading-log level. In cases where a choice of fits was available, we used the authors' preferred set. In order to compare the different predictions, a reference cross section was calculated using the ABFOW (and ABFKW for π^-Be interactions) parton distribution functions evaluated with the scale $Q^2 = p_T^2/4$. The ratios of predicted cross sections relative to the reference cross section for π^0 production are shown in Figs. 30 and 31. The ratios of predicted cross sections relative to the reference cross section for direct-photon production are shown in Figs. 32–35. The ratio of our measured cross sections relative to the reference cross sections are also shown in these figures for $-0.7 < y_{\text{c.m.}} < 0.7$. Similar comparisons in our rapidity subranges yield comparable results.

Figure 30 shows three next-to-leading-log QCD predictions for π^0 production using the parton distribution functions of GRV, ABFKW-ABFOW, and SMRS-MRS for π^-Be interactions. Figure 31 shows five next-to-leading-log QCD predictions for π^0 production using the parton distribution functions of GRV, ABFOW, MRS, and MT for pBe interactions. In each plot the scale is given by $Q^2 = p_T^2/4$. The QCD predictions have been corrected for the measured A dependence for π^0 production. For these plots as well as in subsequent plots, the circles represent our data. Statistical uncertainties are shown by the error bars, while the limits of the systematic uncertainties are given by the triangles. The systematic uncertainties include those presented in the tables, as well as contributions from the uncertainty in the energy scale and beam momentum, all added in quadrature.

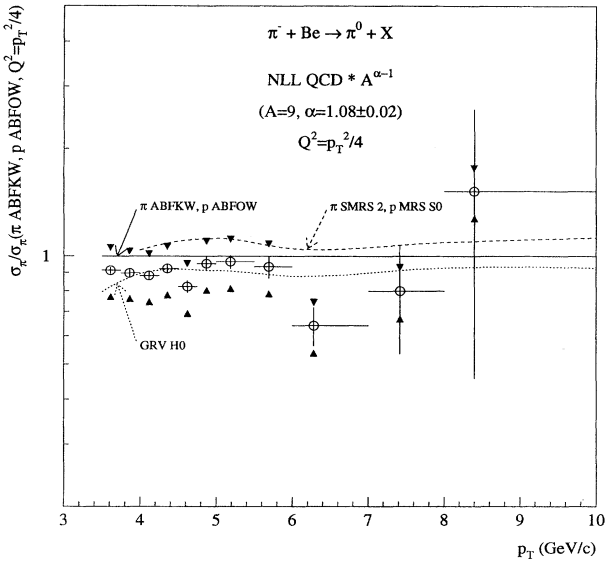

FIG. 30. Comparison of cross sections for π^0 production evaluated using various input parton distribution functions for π^-Be interactions. The reference cross section, by which all other cross sections are divided, is obtained using ABFKW-ABFOW parton distribution functions with the scale $Q^2 = p_T^2/4$. The circles represent our data, also divided by the reference cross section, with statistical uncertainties given by the error bars and systematic uncertainties presented independently of the statistical uncertainties by triangles. The parton distribution functions used in evaluating each cross section are designated next to the corresponding curve. The scale chosen for the evaluation of these cross sections is also $Q^2 = p_T^2/4$. The QCD predictions have been scaled for A dependence using our measured value of α.

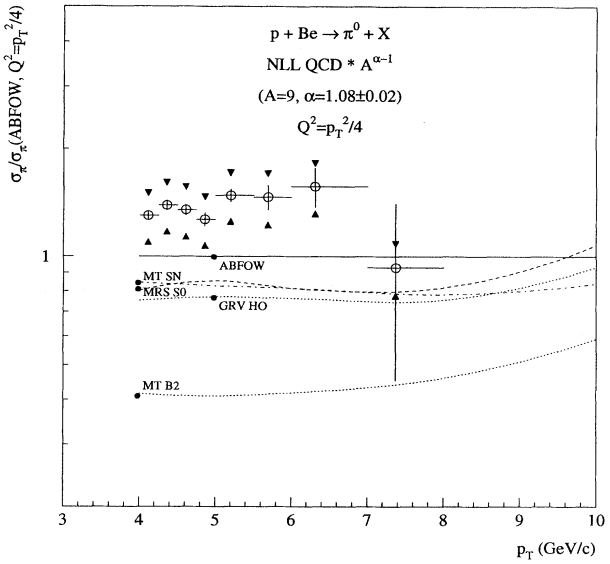

FIG. 31. Comparison of cross sections for π^0 production evaluated using various input parton distribution functions for pBe interactions. The reference cross section for this plot is obtained using ABFOW parton distribution functions with the scale $Q^2 = p_T^2/4$. The circles represent our data, divided by the reference cross section, with statistical uncertainties given by the error bars and systematic uncertainties presented independently of the statistical uncertainties by triangles. The parton distribution functions used in evaluating each cross section are designated next to the corresponding curve. The scale chosen for the evaluation of these cross sections is also $Q^2 = p_T^2/4$. The QCD predictions have been scaled for A dependence using our measured value of α.

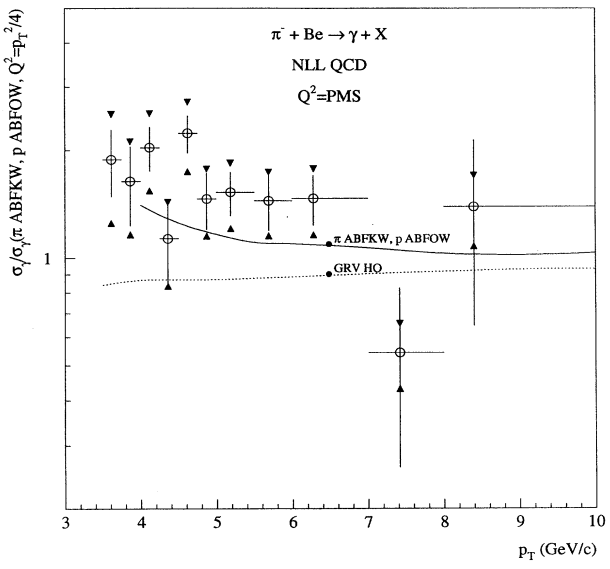

FIG. 32. Comparison of cross sections for direct-photon production evaluated using various input parton distribution functions for π^-Be interactions. The reference cross section is obtained using ABFKW-ABFOW parton distribution functions with the scale $Q^2 = p_T^2/4$. The data is represented as described in Fig. 30. The parton distribution functions used in evaluating each cross section are designated next to the corresponding curve. The scale chosen for the evaluation of these cross sections is determined by PMS.

Figures 32–35 show next-to-leading-log QCD predictions for direct-photon production using various parton distribution functions, for π^-Be and pBe interactions. Figure 32 shows predictions for π^-Be interactions using the parton distribution functions of ABFKW-ABFOW and GRV with the scale determined using PMS. Figure 33 shows predictions for pBe interactions using the parton distribution functions of ABFOW and GRV with the scale determined using PMS and with different values of η_g for the ABFOW parton distribution functions; where the gluon distribution function is parametrized as $xG(x, Q_0^2 = 2) = A_g(1-x)^{\eta_g}$, with A_g and η_g being parameters. The set labeled by $\eta_g = 3.9$ is the best fit of Ref. [20] to WA70 and BCDMS data. The sets labeled by $\eta_g = 3$ and $\eta_g = 5$ show the sensitivity of the predicted cross section to the behavior of the gluon distribution function. The predicted cross sections at large p_T in Fig. 33 decrease with increasing values of η_g due to the greater suppression of the gluon contribution in this x range. As can be seen, the difference in cross sections between $\eta_g = 3$ and $\eta_g = 3.9$ is of the order of 35% for $p_T < 6$ GeV.

Figure 34 shows the predicted cross sections for π^-Be interactions using the parton distribution functions of ABFKW-ABFOW, GRV, and SMRS-MRS for the fixed scale $Q^2 = p_T^2/4$. Figure 35 shows the predicted cross sections for pBe interactions using the parton distribution functions of ABFOW, GRV, MRS, and MT for the same scale. From these figures we see that the QCD expectations evaluated at the next-to-leading order vary by as much as a factor of 2, depending on the chosen set of

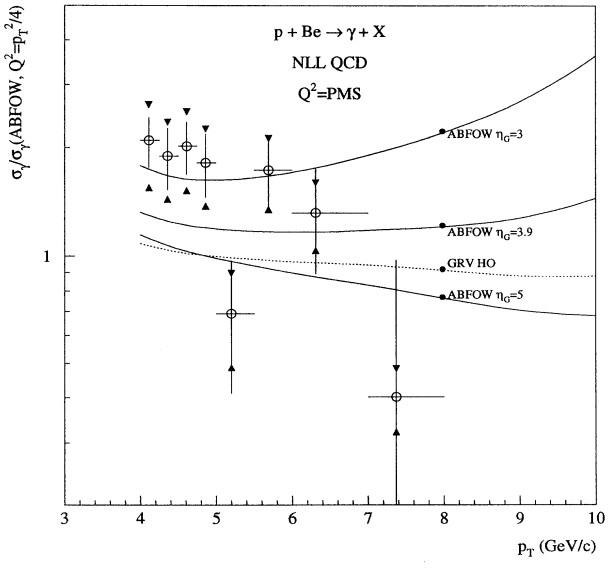

FIG. 33. Comparison of cross sections for direct-photon production evaluated using various input parton distribution functions for pBe interactions. The reference cross section is obtained using ABFOW parton distribution functions with the scale $Q^2 = p_T^2/4$. The data is represented as described in Fig. 30. The parton distribution functions used in evaluating each cross section are designated next to the corresponding curve. The scale chosen for the evaluation of these cross sections is determined by PMS.

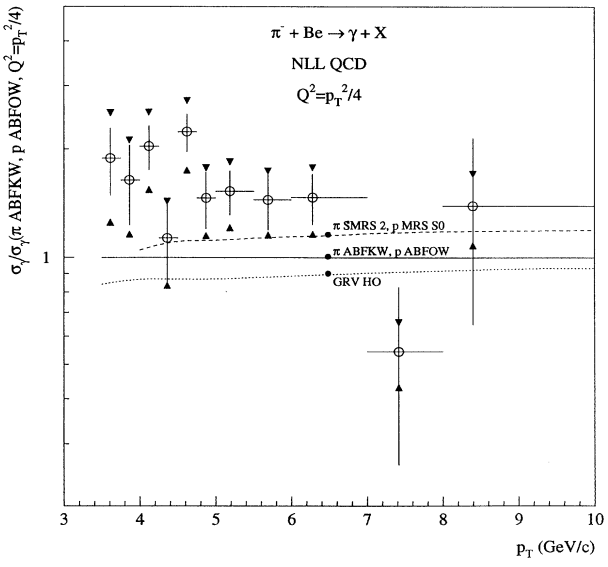

FIG. 34. Comparison of cross sections for direct-photon production evaluated using various input parton distribution functions for π^-Be interactions. The reference cross section is the same as in Fig. 32. The data is represented as described in Fig. 30. The parton distribution functions used in evaluating each cross section are designated next to the corresponding curve. The scale chosen for the evaluation of these cross sections is $Q^2 = p_T^2/4$.

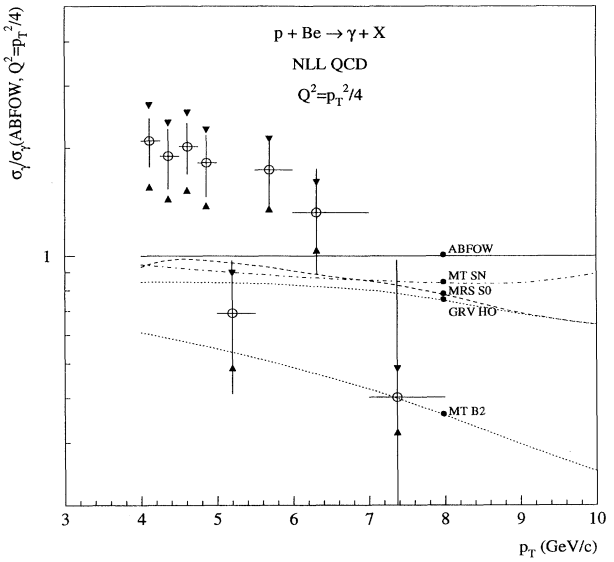

FIG. 35. Comparison of cross sections for direct-photon production evaluated using various input parton distribution functions for pBe interactions. The reference cross section is the same as in Fig. 33. The data is represented as described in Fig. 30. The parton distribution functions used in evaluating each cross section are designated next to the corresponding curve. The scale chosen for the evaluation of these cross sections is $Q^2 = p_T^2/4$.

parton distribution functions, the definitions used for Q^2, and the p_T range considered.

Several sets of parton distribution functions have been published by Martin *et al.* [29] which are intended to reflect current uncertainties in the determination of the distribution functions using a consistent fitting procedure and data sample. Using these parton distribution functions to gauge the uncertainty in the predicted next-to-leading-log cross sections yields a spread similar to that shown in Figs. 30–35.

The agreement between the different expectations is generally good when the cross sections are calculated using the same factorization scale; however, the data favor choices of scale $< p_T^2/4$. The best agreement with the data is obtained using the ABFKW parton distribution functions for π^- and the ABFOW parton distribution functions for nucleons, with the choice of factorization determined through PMS.

V. SUMMARY

The invariant cross sections for π^0, η, and direct-photon production have been measured for pBe and π^-Be collisions as a function of p_T and $y_{\text{c.m.}}$. The π^0 and direct-photon cross sections have been compared with next-to-leading-log expectations from QCD. When the π^0 cross sections per nucleon are fitted to the form A^α we obtain a value for α of 1.08 ± 0.02 for π^0 production from Be and Cu targets. Comparisons between our data and predictions from QCD at next-to-leading order were made using several sets of parton distribution functions. Current experimental uncertainties limit our ability to distinguish among these sets.

ACKNOWLEDGMENTS

We wish to thank the U.S. Department of Energy, the National Science Foundation, including its Office of International Programs, the Universities Grants Commission of India, and Fermilab for their support of this research. We are also pleased to acknowledge the contributions of our colleagues on Fermilab experiment E672. We would also like to thank P. Aurenche, R. Baier, J. P. Guillet, J. Morfín, J. Owens, J. Qiu, W. Tung, and M. Werlen for many helpful discussions and for providing us with their QCD calculations. In addition we wish to thank the following colleagues for their invaluable help in the construction and operation of the Meson West spectrometer: W. Dickerson from Northeastern University; D. Andreuzzi, J. Bloomquist, G. Borchardt, J. Clark, J. Collins, P. Constanta, D. Cosgrove, P. Deering, G. Deuerling, C. Dong, G. Drake, R. Hiller, K. Jenkins, K. Kephart, H. Koecher, E. Lavallie, P. Madsen, B. Maly, G. Olsen, D. Petravick, C. Richardson, J. Sasek, R. Tokarek, K. Turner, J. Tweed, J. Western, and D. Quintero from Fermilab; E. Buchanan, R. Cucil, J. Eyngorn, T. Haelen, D. Kasper, L. Kuntz, and F. Viggiani from the University of Rochester; H. Wright, P. Wright, and R. Wright, from Michigan State University; A. Jain and D. Kaul from University of Delhi; V. McAnulty and J. Passaneau from Pennsylvania State University.

[1] W. M. Geist *et al.*, Phys. Rep. **197**, 263 (1990).
[2] N. A. McCubbin, Rep. Prog. Phys. **44**, 1027 (1981).
[3] T. Ferbel and W. Molzon, Rev. Mod. Phys. **56**, 181 (1984); E. Berger, E. Braaten, and R. Field, Nucl. Phys. B **239**, 52 (1984); J. F. Owens, Rev. Mod. Phys. **59**, 465 (1987); L. Camilleri, in *Proceedings of the XIXth International Symposium on Multiparticle Dynamics*, Arles, France, 1988, edited by D. Schiff and J. Tran Thanh Van (Editions Frontières, Gif-sur-Yvette/World Scientific, Singapore, 1988), p. 203; J. Huston, in *Proceedings of the XIVth International Symposium on Lepton and Photon Interactions*, Stanford, California, 1989, edited by M. Riordan (World Scientific, Singapore, 1990), p. 348.
[4] P. Aurenche *et al.*, Phys. Lett. **140B**, 87 (1984); P. Aurenche *et al.*, Nucl. Phys. **B286**, 509 (1987); P. Aurenche *et al.*, *ibid.* **B297**, 661 (1988).
[5] Collider Detector at Fermilab Collaboration, F. Abe *et al.*, Phys. Rev. Lett. **68**, 2734 (1992); UA1 Collaboration, C. Albajar *et al.*, Phys. Lett. B **209**, 385 (1988); UA2 Collaboration, R. Ansari *et al.*, Z. Phys. C **41**, 395 (1988); UA2 Collaboration, J. Alitti *et al.*, Phys. Lett. B **263**,

544 (1991).
[6] CCOR Collaboration, A. L. S. Angelis *et al.*, Phys. Lett. **94B**, 106 (1980); R806 Collaboration, E. Anassontzis *et al.*, Z. Phys. C **13**, 277 (1982); CMOR Collaboration, A. L. S. Angelis *et al.*, Nucl. Phys. **B327**, 541 (1989); AFS Collaboration, E. Anassontzis *et al.*, Yad. Fiz. **51**, 1314 (1990) [Sov. J. Nucl. Phys. **51**, 836 (1990)].
[7] E629 Collaboration, M. McLaughlin *et al.*, Phys. Rev. Lett. **51**, 971 (1983); NA3 Collaboration, J. Badier *et al.*, Z. Phys. C **31**, 341 (1986); NA24 Collaboration, C. DeMarzo *et al.*, Phys. Rev. D **36**, 8 (1987); WA70 Collaboration, M. Bonesini *et al.*, Z. Phys. C **37**, 535 (1988); WA70 Collaboration, M. Bonesini *et al.*, *ibid.* **38**, 371 (1988); UA6 Collaboration, A. Bernasconi *et al.*, Phys. Lett. B **206**, 163 (1988).
[8] G. Alverson *et al.*, Phys. Rev. Lett. **68**, 2584 (1992); G. Alverson *et al.*, Phys. Rev. D **45**, R3899 (1992).
[9] V. Abramov *et al.*, Fermilab Report No. Pub-91/62-E, 1991 (unpublished).
[10] I. Kourbanis, Ph.D. thesis, Northeastern University, 1989.
[11] E. Engels, Jr. *et al.*, Nucl. Instrum. Methods A **279**, 272 (1989).
[12] K. Hartman, Ph.D. thesis, Pennsylvania State University, 1990.
[13] F. Lobkowicz *et al.*, Nucl. Instrum. Methods A **235**, 332 (1985).
[14] G. Drake *et al.*, Nucl. Instrum. Methods A **269**, 68 (1988).
[15] Fermilab Computing Department, ACP Software User's Guide (Fermilab GA001, Batavia, IL, 1988).
[16] R. Brun *et al.*, GEANT3: CERN Data Handling Division, DD/EE/84-1, 1987.
[17] M. Diakonou *et al.*, Phys. Lett. **89B**, 432 (1980); G. Donaldson *et al.*, Phys. Rev. D **21**, 828 (1980); A. Chilingarov *et al.*, Nucl. Phys. **B151**, 29 (1979).
[18] H. U. Bengtsson and T. Sjöstrand, Comput. Phys. Commun. **46**, 43 (1987); H. U. Bengtsson and G. Ingelman, *ibid.* **34**, 251 (1985); H. U. Bengtsson, *ibid.* **31**, 323 (1984).
[19] F. Aversa *et al.*, Nucl. Phys. **B327**, 105 (1989).
[20] P. Aurenche *et al.*, Phys. Rev. D **39**, 3275 (1989); P. Aurenche *et al.*, Phys. Lett. B **233**, 517 (1989).
[21] D. Antreasyan *et al.*, Phys. Rev. D **19**, 764 (1979); H. J. Frisch *et al.*, *ibid.* **27**, 1001 (1983).
[22] P. B. Straub *et al.*, Phys. Rev. Lett. **68**, 452 (1992).
[23] G. J. Donaldson *et al.*, Phys. Rev. Lett. **40**, 684 (1978); R806 Collaboration, C. Kourkoumelis *et al.*, Phys. Lett. **84B**, 277 (1979); E629 Collaboration, J. Povlis *et al.*, Phys. Rev. Lett. **51**, 967 (1983); AFS Collaboration, T. Åkesson *et al.*, Phys. Lett. **158B**, 282 (1985); UA2 Collaboration, M. Banner *et al.*, Z. Phys. C **27**, 329 (1985); UA6 Collaboration, J. Antille *et al.*, Phys. Lett. B **194**, 568 (1987); WA70 Collaboration, M. Bonesini *et al.*, Z. Phys. C **42**, 527 (1989); Collider Detector at Fermilab Collaboration, F. Abe *et al.*, Phys. Rev. Lett. **68**, 2734 (1992).
[24] The general concept of PMS is described by P. M. Stevenson and H. David Politzer, Nucl. Phys. **B277**, 758 (1986), while its application to direct-photon cross sections is discussed by P. Aurenche *et al.*, *ibid.* **B286**, 509 (1987).
[25] M. Glück, E. Reya, and A. Vogt, Z. Phys. C **53**, 127 (1992); **53**, 651 (1992).
[26] A. D. Martin, R. G. Roberts, and W. J. Stirling, Phys. Rev. D **47**, 867 (1993).
[27] J. G. Morfín and W. K. Tung, Z. Phys. C **52**, 13 (1991).
[28] P. J. Sutton, A. D. Martin, R. G. Roberts, and W. J. Stirling, Phys. Rev. D **45**, 2349 (1992).
[29] A. D. Martin, R. G. Roberts, and W. J. Stirling, Phys. Rev. D **43**, 3648 (1991).